The Planetary Science Journal, 2:155 (19pp), 2021 August https://doi.org/10.3847/PSJ/ac139e

No Activity among 13 Centaurs Discovered in the Pan-STARRS1 Detection Database

Eva Lilly[1], Henry Hsieh[1], James Bauer[2], Jordan Steckloff[1,3], Peter Jevčák[4], Robert Weryk[5], Richard J. Wainscoat[5], and Charles Schambeau[6]
[1] Planetary Science Institute, 1700 E. Fort Lowell, Suite 106, Tucson, AZ 85719-2395, USA; elilly@psi.edu
[2] University of Maryland, College Park, MD 20742-2421, USA
[3] University of Texas at Austin, Austin, TX 78712, USA
[4] Comenius University, Mlynská dolina, 842 48 Bratislava, Slovakia
[5] Institute for Astronomy, University of Hawaii, 2680 Woodlawn Drive, Honolulu, HI 96822, USA
[6] University of Central Florida, 4000 Central Florida Boulevard, Orlando, FL 32816, USA
Received 2021 April 26; revised 2021 June 28; accepted 2021 July 11; published 2021 August 10

Abstract

Centaurs are small bodies orbiting in the giant planet region that were scattered inward from their source populations beyond Neptune. Some members of the population display comet-like activity during their transition through the solar system, the source of which is not well understood. The range of heliocentric distances where the active Centaurs have been observed and their median lifetime in the region suggest that this activity is driven neither by water-ice sublimation nor entirely by supervolatiles. Here we present an observational and thermodynamical study of 13 Centaurs discovered in the Pan-STARRS1 detection database aimed at identifying and characterizing active objects beyond the orbit of Jupiter. We find no evidence of activity associated with any of our targets at the time of their observations with the Gemini North telescope in 2017 and 2018, or in archival data from 2013 to 2019. Upper limits on the possible volatile and dust production rates from our targets are 1–2 orders of magnitude lower than production rates in some known comets and are in agreement with values measured for other inactive Centaurs. Our numerical integrations show that the orbits of six of our targets evolved interior to $r \sim 15$ au over the past 100,000 yr, where several possible processes could trigger sublimation and outgassing, but their apparent inactivity indicates that either their dust production is below our detection limit or the objects are dormant. Only one Centaur in our sample—2014 PQ_{70}—experienced a sudden decrease in semimajor axis and perihelion distance attributed to the onset of activity for some previously known inactive Centaurs, and therefore it is the most likely candidate for any future outburst. This object should be a target of high interest for any further observational monitoring.

Unified Astronomy Thesaurus concepts: Centaur group (215); Comets (280); Trans-Neptunian objects (1705)

1. Introduction

Centaurs are small bodies most commonly defined as having perihelia (q) and semimajor axes (a) between the orbits of Jupiter and Neptune, i.e., 5.2 au $< q$, $a <$ 30 au (e.g., Jewitt 2009), which are migrating toward the inner solar system from their source regions in trans-Neptunian space. Once a trans-Neptunian object (TNO) evolves to within Neptune's orbit and becomes a Centaur, it enters a chaotic, gravitational pinball machine where it is rapidly passed between the gravitational influences of the giant planets. Centaurs eventually leave the region via several routes—they collide with one of the planets, they return back to the trans-Neptunian region or even get ejected from the solar system, or about 20% of Centaurs enter an end state as a Jupiter-family comet (JFC; Volk & Malhotra 2008; Sarid et al. 2019). Due to the chaotic gravitational environment, the typical dynamical lifetime of a Centaur is only ~10 Myr (Tiscareno & Malhotra 2003; Di Sisto & Brunini 2007). In this way, the Centaur population delivers useful clues of the pristine composition and physical properties of small TNOs beyond our current observational limits right to our doorstep.

One of the most puzzling characteristics of Centaurs is comet-like activity exhibited by ~5% of the population (Chandler et al. 2020). Unlike in most short-period comets, this activity is not water driven because the majority of active Centaurs reside at large heliocentric distances where the surface temperatures are too low to allow for water-ice sublimation (Meech & Svoren 2004; Womack et al. 2017). Active Centaurs also show a variety of behaviors, from long-term low-level outgassing, such as in (2060) 95P/Chiron (Luu & Jewitt 1990; Foster et al. 1999), to sudden violent outbursts in previously known dormant objects, as observed in 174P/Echeclus (Choi et al. 2006; Bauer et al. 2008; Rousselot 2008; Kareta et al. 2019; Seccull et al. 2019), and unlike in regular comets, the timing of the activity onset is not obviously centered on perihelion. Dust production rates often range by orders of magnitudes from one object to another, and the source of this activity remains unknown. Most known Centaurs have spent the majority of their lifetime in regions too warm to maintain surface supplies of supervolatile ices such as CO and CO_2 (Jewitt 2009), for example, if free CO ice were present on all Centaurs, we should observe Centaurs with comae well beyond the orbit of Neptune, just like in some long-period comets (e.g., Szabó et al. 2008; Meech et al. 2017), which is not the case. Multiple works have shown that there are no known active Centaurs beyond $r \sim 14$ au and that the lack of activity cannot simply be attributed to observational selection effects (Jewitt 2009; Cabral et al. 2019; Li et al. 2020). The fraction of active objects among Centaurs with perihelia smaller than 14 au is almost 20%, while only 10% of Centaurs are active within the overall population. Moreover, almost 27% of all active

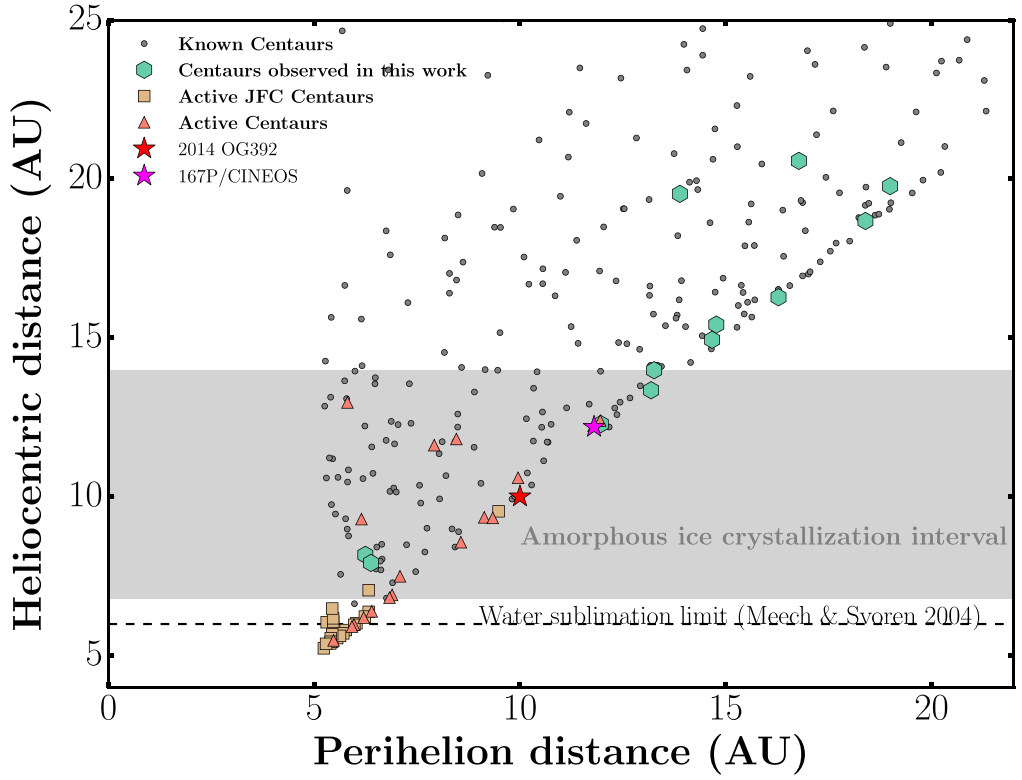

Figure 1. Perihelion distance vs. heliocentric distance of 13 Centaurs studied in this work compared to known active Centaurs and JFC Centaurs, as well as the known Centaur population. All known active Centaurs reside within the interval where the crystallization of AWI is possible. Our targets are distributed both within and beyond the crystallization interval. A magenta star marks the position of 167P/CINEOS, which shares a similar orbit and heliocentric position at the time of activity to those of one of the Centaurs in our sample, 2014 OX_{393}.

Centaurs have perihelia smaller than 6.5 au, as can be seen in Figure 1.

Therefore, considering the wide range of heliocentric distances at which Centaurs exhibit comae, the Centaur activity likely has more sources than just sublimation of surface volatiles, and these sources may be triggered by multiple mechanisms, some of which could be different from those acting in regular comets.

It has been suggested that activity on Centaurs and some comets at large heliocentric distances is driven by the crystallization of amorphous water ice (AWI), which is porous and can contain molecules of supervolatile ices trapped in the AWI during the condensation (Notesco & Bar-Nun 1996; Jewitt 2009; Shi & Ma 2015). When the parent body enters a warmer environment, a crystallization front starts propagating into the interior of the body, releasing trapped gas molecules, which then start to loft dust grains at temperatures much lower than necessary for sublimation of crystalline water ice. AWI has been detected by in situ observation of the Galilean moons of Jupiter (Hansen & McCord 2004); however, the presence of AWI has never been observationally confirmed on small bodies in the solar system (Lisse et al. 2013).

The phase transition of AWI to crystalline water ice has been proposed to start at a heliocentric distance of $r \sim 7$ au (Jewitt 2009; Womack et al. 2017), while recent thermal modeling studies show that it can be triggered up to $r \sim 14$ au, with some extreme cases crystallizing as far as $r \sim 16$ au (Guilbert-Lepoutre 2012). Figure 1 shows that the known active Centaurs indeed have perihelia within this heliocentric distance range, which could support the idea of AWI crystallization as their main activity driver. However, Figure 1 also shows that there are other apparently inactive bodies with very similar orbital parameters. Thus, the mere presence of AWI, which should be abundant in TNOs and Centaurs (Jenniskens & Blake 1994), does not appear to be enough on its own for an object to exhibit activity, indicating that activity may require a certain trigger. Fernández et al. (2018) suggested that a rapid change in the thermal environment of the body could jump-start AWI crystallization in a dormant object. Such an orbital change could be caused by a close encounter with a planet and subsequent decrease of perihelion or semimajor axis, which is believed to have led to outbursts in several Centaurs and the previously dormant quasi-Hilda P/2010 H2 (Vales) (e.g., Mazzotta Epifani et al. 2006; Fernández et al. 2018; Jewitt & Kim 2020).

Another plausible explanation for increased activity in Centaurs that have been only recently scattered inward would be the sublimation of subsurface pockets of CO_2 and other supervolatile ices. CO_2 in particular is significantly more volatile than water ice, and it is one of the most common species found on cometary bodies (e.g., Bockelée-Morvan et al. 2004; A'Hearn et al. 2011). Thermal models show that it can sublime vigorously interior to ~15 au (Steckloff et al. 2015; Meech et al. 2017), which coincides closely with the heliocentric distances of observed Centaur activity. Such subsurface deposits could be forcefully exposed by some external force and start to rapidly sublimate. We can rule out impacts as the predominant surface activity trigger on Centaurs owing to the very low collision rate in the region (Durda & Stern 2000), but other forces might play a role. For example, Steckloff et al. (2016) have shown that topographic features on the surface of comets, when steeper than ~30°, are prone to mass wasting events that can excavate buried volatiles such as CO and CO_2 to the surface.

Table 1
Observing Geometry, Time of Observation, and Photometry

Name	UT Date	Δ[a]	r[b]	α[c]	FWHM	Air Mass	Φ[d]	m_r[e]
2013 MZ_{11}	2017 Sep 24	19.8	20.6	1.8	0.76	1.75	4.74	21.24 ± 0.02
2014 NX_{65}	2017 Sep 24	17.7	18.7	0.8	0.62	1.21	3.37	22.00 ± 0.23
2014 TV_{85}	2017 Dec 11	14.6	14.9	3.5	0.67	1.07	4.05	21.26 ± 0.02
2015 BD_{518}	2017 Nov 14	16.5	16.3	3.4	0.73	1.31	2.00	21.93 ± 0.03
2015 BH_{518}	2017 Dec 30	25.1	25.4	2.1	0.76	1.15	4.05	22.60 ± 0.07
2014 WW_{508}	2017 Nov 17	13.3	14.0	3.4	0.67	1.02	3.37	22.17 ± 0.03
2010 TU_{191}	2018 Jan 16	14.8	15.5	2.1	1.05	1.31	3.37	22.81 ± 0.04
2014 JD_{80}	2017 Sep 19	19.2	19.8	2.2	1.54	1.70	4.00	21.83 ± 0.04
2014 OX_{393}	2017 Nov 9	11.3	12.3	0.6	0.69	1.48	4.05	21.63 ± 0.02
2014 YX_{49}	2017 Nov 11	19.3	19.6	2.7	0.62	1.04	2.50	21.66 ± 0.02
2014 WX_{508}	2017 Dec 11	13.4	13.4	3.9	0.63	1.16	4.05	22.32 ± 0.10
2015 BK_{518}	2018 Jan 17	7.9	8.1	6.8	1.13	1.25	8.16	23.71 ± 0.12
2014 PQ_{70}	2017 Sep 23	7.2	8.1	6.6	1.11	1.39	7.47	24.02 ± 0.14

Notes.
[a] Geocentric distance, au.
[b] Heliocentric distance, au.
[c] Solar phase angle, deg.
[d] Angular diameter of photometry aperture, arcseconds.
[e] Measured mean apparent r'-band magnitude.

An important aspect to consider is also the time an object has already spent in the Centaur region, or the past changes in its orbit pushing its orbit within the AWI crystallization limit or past the point where the sublimation of other supervolatiles is possible. In general, it is expected that the active Centaurs have young orbits, i.e., they have only recently entered the region, since the timescale on which the crystallization front is able to propagate before it depletes the AWI supplies is fairly small (on order of 10^5 yr; Guilbert-Lepoutre 2012), and also the depletion of the CO layers is rapid (Li et al. 2020).

CO has been detected in the comae of several Centaurs (e.g., Womack & Stern 1997; Wierzchos et al. 2017; Womack et al. 2017), while CO_2, which is notoriously challenging to detect with ground-based assets, has only been observed in comets so far (Ootsubo et al. 2012; Womack et al. 2017). It is unclear whether the observed production rates were caused by gases released during the AWI phase transition or from sublimation of subsurface supervolatile ice pockets. Therefore, to better understand the types of activities displayed in the Centaur region, we need to gain a more informed and complex view of the orbital and thermal histories of Centaurs and the current status of their volatile content.

Observations for this work have been collected in the framework of a long-term program aimed at searching for active Centaurs and analyzing their orbital and thermal environment. Here we present the analysis of our pilot study on a sample of 13 Centaurs that were discovered in the detection database of the Panoramic Survey Telescope and Rapid Response System survey (Pan-STARRS1; Weryk et al. 2016).

2. Methods

In this work we have observed and analyzed 13 Centaurs discovered in the Pan-STARRS1 detection database (Weryk et al. 2016). All our targets have well-defined orbits with orbital arcs spanning almost a decade. Our investigation consisted of three steps: (1) analysis of images taken with Gemini-N to search for comet-like activity, (2) a search of archival images from the Dark Energy Camera (DECam) to look for traces of activity in the past, (3) thermal modeling to examine surface temperatures as a function of orbital parameters and object size to put upper limits on sublimative gas production from volatile species potentially present on the surface, and (4) numerical integrations to inspect the orbital histories of objects in our sample.

2.1. Observations and Data Reduction

We observed our targets with the GMOS-N (Gemini Multi-Object Spectrograph) instrument on the Gemini North telescope on Maunakea, Hawaii, between 2017 August 1 and 2018 January 31 (No. GN-2017B-Q-69). GMOS-N has a $300'' \times 300''$ field of view and a pixel scale of $0\farcs0728$ pixel^{-1}. For our observations, we used the imaging mode of GMOS-N with 2×2 binning and a Sloan Digital Sky Survey (SDSS) r' filter (Fukugita et al. 1996), which is ideal for detecting dust (Meech & Svoren 2004). We employed nonsidereal tracking at the apparent rate and direction of motion for each target and acquired sequences of three 100 s exposures, which were necessary to correctly identify each target based on their motion. All our observations were done in queue mode, meaning that each object was observed under slightly different conditions throughout the semester. Our observations are summarized in Table 1.

Standard bias subtraction, flat-field correction, and cosmic-ray removal were performed for all images using the Python 3 code utilizing the `ccdproc` package in Astropy[7] (Astropy Collaboration et al. 2018) and the `L.A.Cosmic` Python module[8] (van Dokkum 2001; van Dokkum et al. 2012). Images from each night were aligned on the object and co-added together to create composite images using IRAF software (Tody 1986, 1993) in order to maximize signal-to-noise ratio (S/N). Absolute photometric calibration was carried out using a photometry pipeline developed by Mommert (2017), standard IRAF routines, and the all-sky ATLAS-REFCAT2 catalog (Tonry et al. 2018).

[7] http://www.astropy.org
[8] Written for Python by Maltes Tewes (https://github.com/RyleighFitz/LACosmics).

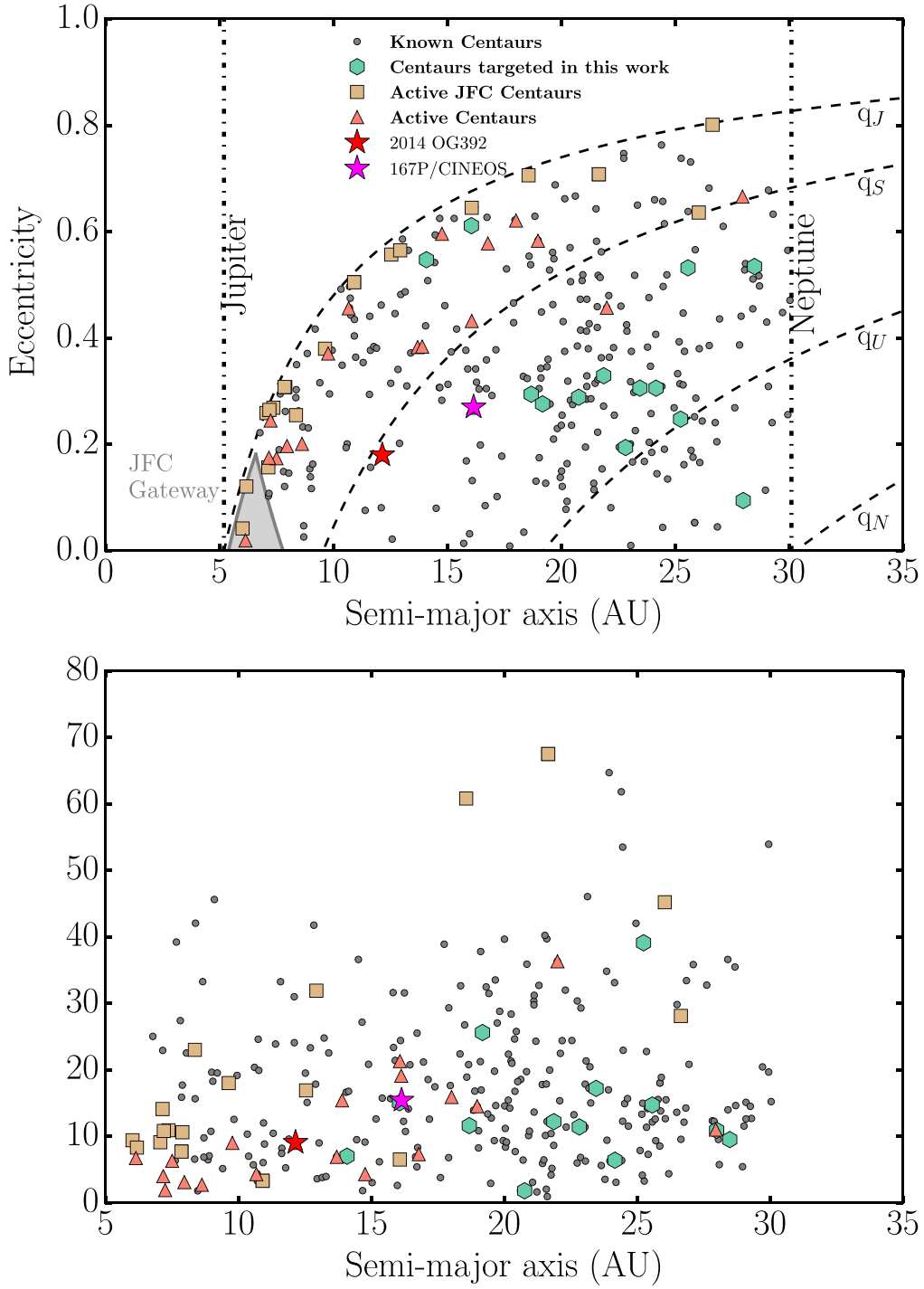

Figure 2. Semimajor axis vs. eccentricity (top panel) and semimajor axis vs. inclination (bottom panel) of our targets compared to known active Centaurs and JFC Centaurs, as well as the known Centaur population. Dashed curves represent the loci of orbits with perihelia equal to those of perihelia of giant planets, and dashed–dotted lines show semimajor axes of Jupiter and Neptune that border the Centaur region. The filled gray triangle represents the JFC Gateway region according to Sarid et al. (2019).

2.1.1. Target Selection

Our target list consisted of 13 Centaurs selected from a sample of 29 new Centaur discoveries from the Pan-STARRS1 detection catalog (Weryk et al. 2016) that were observable in the second half of 2017 from the Northern Hemisphere and were within Gemini-N observation limits. We included objects with perihelia spanning the entire Centaur region and crossing the putative AWI crystallization heliocentric distance interval (Jewitt 2009; Guilbert-Lepoutre 2012). Most of the known active Centaurs were discovered close to perihelion and were active at discovery. We therefore primarily selected targets close to perihelion to ensure the best conditions for observing possible activity. As of 2021 June none of our targets have been the subject of characterization by other works.

Figures 1 and 2 show that our targets cover a wide range of orbital elements typical for Centaurs and stay clear of the region often referred to as the "JFC Gateway," a temporary low-eccentricity region exterior to Jupiter through which the majority

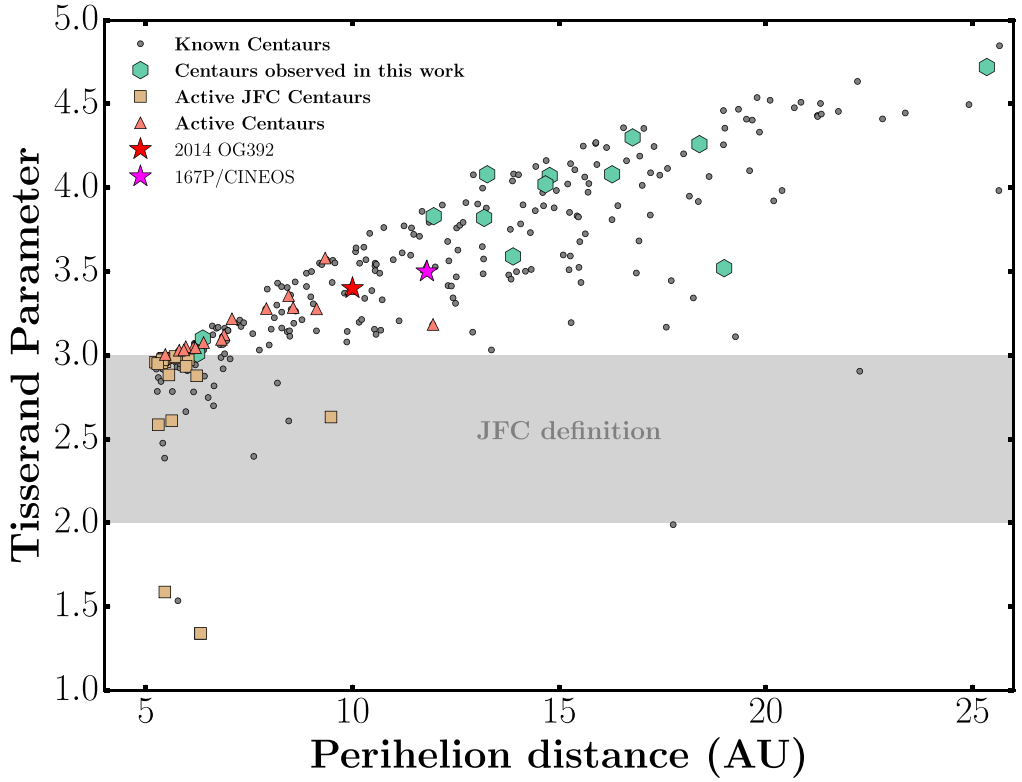

Figure 3. Perihelion distance vs. Tisserand parameter with respect to Jupiter of 13 Centaurs studied in this work compared to known active Centaurs and JFC Centaurs, as well as the known Centaur population as of 2021 February.

Table 2
Orbital Parameters

Name	q[a]	a[b]	e[c]	i[d]	M[e]	T_J[f]	T_S[g]	T_U[h]
2013 MZ_{11}	16.828	24.228	0.305	6.40	314.40	4.30	3.41	2.92
2014 NX_{65}	18.386	22.868	0.196	11.40	16.30	4.26	3.39	2.94
2014 TV_{85}	14.653	21.796	0.328	12.20	348.40	4.02	3.22	2.85
2015 BD_{518}	16.277	23.383	0.304	17.20	359.20	4.08	3.25	2.83
2015 BH_{518}	25.356	27.954	0.093	10.90	9.70	4.72	3.68	3.05
2014 WW_{508}	13.259	28.219	0.53	9.50	8.20	4.08	3.21	2.71
2010 TU_{191}	14.764	20.65	0.285	1.80	19.10	4.07	3.28	2.92
2014 JD_{80}	19.012	25.318	0.249	39.10	337.90	3.52	2.82	2.48
2014 OX_{393}	11.963	25.444	0.53	14.70	5.60	3.83	3.05	2.64
2014 YX_{49}	13.825	19.113	0.277	25.60	78.10	3.59	2.95	2.73
2014 WX_{508}	13.173	18.631	0.293	11.60	348.90	3.82	3.13	2.88
2015 BK_{518}	6.393	14.258	0.552	7.00	16.50	3.10	2.69	2.77
2014 PQ_{70}	6.25443	16.037	0.6	15.04	11.80	3.01	2.58	2.60

Notes.
[a] Perihelion distance, au.
[b] Semimajor axis, au.
[c] Orbital eccentricity.
[d] Inclination, degrees.
[e] Mean anomaly at the time of observation, degrees.
[f] Tisserand's parameter with respect to Jupiter.
[g] Tisserand's parameter with respect to Saturn.
[h] Tisserand's parameter with respect to Uranus.

of Centaurs bound to become JFCs pass (Sarid et al. 2019; Steckloff et al. 2020). In contrary, most objects in our sample have perihelia near the upper limit of the AWI crystallization zone because the data-mining algorithm applied to the Pan-STARRS1 detection database was tuned to find objects beyond Neptune and the discovered Centaurs were mostly a by-product of that search (Weryk et al. 2016). It can also be seen that the activity in Centaurs does not seem to be related to any preferential eccentricity or inclination ranges, but instead their perihelion distances appear to be the main constraint.

By definition, JFCs orbiting in the same region as the Centaurs (i.e., 5.2 au $< q$, $a < 30$ au) differ only by the fact that

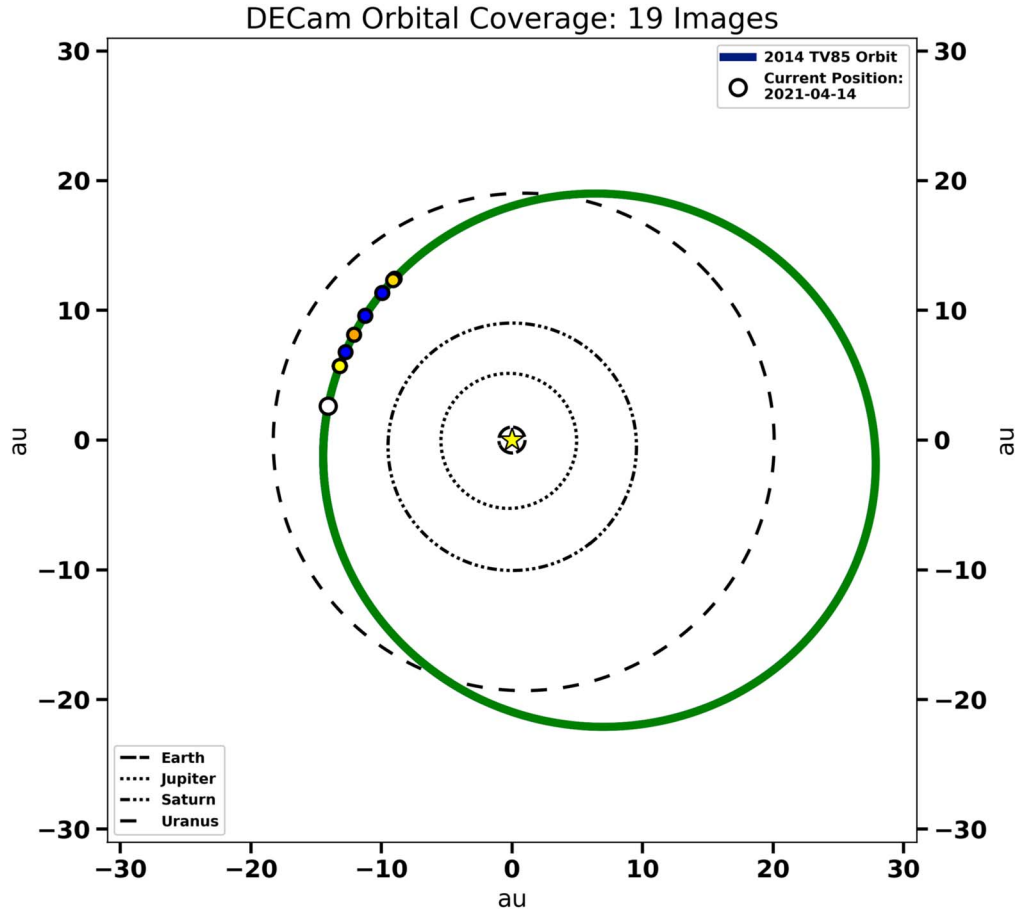

Figure 4. Orbital image coverage of 2014 TV_{85} from the DECam archival images. The colored circles on the Centaur's orbit indicate the orbital locations for which there are DECam images. There were a total of 19 archival DECam images of the object, out of which 8 were suited for calibration. The calibrated data span 4 yr (2014–2018).

they are active, and in terms of Tisserand's parameter with respect to Jupiter, T_J, which is given by

$$T_J = a_J/a + 2\cos i\sqrt{a/a_J(1-e^2)}, \quad (1)$$

where a_J is the semimajor axis of Jupiter and a, e, and i are the semimajor axis, eccentricity, and inclination of the Centaur, respectively. JFCs have $2 > T_J > 3$ and perihelia below ~6 au, while Centaurs typically have larger T_J and larger perihelia, signaling that their orbits are decoupled from Jupiter (Fernández et al. 2018). To add to the confusion, the Gateway objects are by definition Centaurs, but their orbits are not decoupled from Jupiter, while there also are inactive Centaurs with $T_J < 3$ in the population. Objects with perihelia between 5.2 and 6 au are thus on the border of these two classes, and they often make trips to within Jupiter's orbit and back to the Centaur region—the typical example being the famous Gateway Centaur 2019 LD_2 (Steckloff et al. 2020). Therefore, we use the term "JFC Centaurs" throughout this paper for addressing these borderline active objects. There are a total of 18 active Centaurs and 21 JFC Centaurs known in the region as of 2021 February 10.[9]

We have also calculated Tisserand's parameter with respect to Saturn and Uranus, T_S and T_U, respectively, and Table 2 shows that about half of our targets are likely more influenced by the outer planets than Jupiter. The current values of T_J of our targets and other bodies in the region are plotted against their perihelion distance and are shown in Figure 3. Again, we do not note any apparent correlation between activity and T_J.

2.2. Archival Search

We used the Canadian Astronomy Data Centre's Solar System Object Image Search (Gwyn et al. 2012) to search the Dark Energy Survey (DES; Abbott et al. 2018) archive for serendipitous observations of our 13 Centaurs from the DECam (Flaugher et al. 2015) installed on the Cerro Tololo Inter-American Observatory's Blanco 4 m telescope. The DECam instrument consists of 62 individual 2 × 4k CCDs for imaging in a hexagonal arrangement on the focal plane. This results in a 2.°2-diameter field of view and 0.″263 $pixel^{-1}$ plate scale. The combination of a relatively large field of view and the deep imaging afforded by the Blanco telescope results in a treasure trove of serendipitously imaged solar system small bodies using DECam. Such a search yielded the recent discovery of an active Centaur, 2014 OG_{392} (Chandler et al. 2020).

Since the archival data we used only cover observation epochs between ~2013 and 2019, they do not provide significant orbital coverage of a typical Centaur orbit, as their orbital periods are several decades to several hundred years long. However, these archival data are still useful as snapshot observations to search for possible activity. For reference, Figure 4 shows the orbital arc of one of our Centaur targets (2014 TV_{85}) that is covered by data from DECam.

[9] https://physics.ucf.edu/~yfernandez/cometlist.html

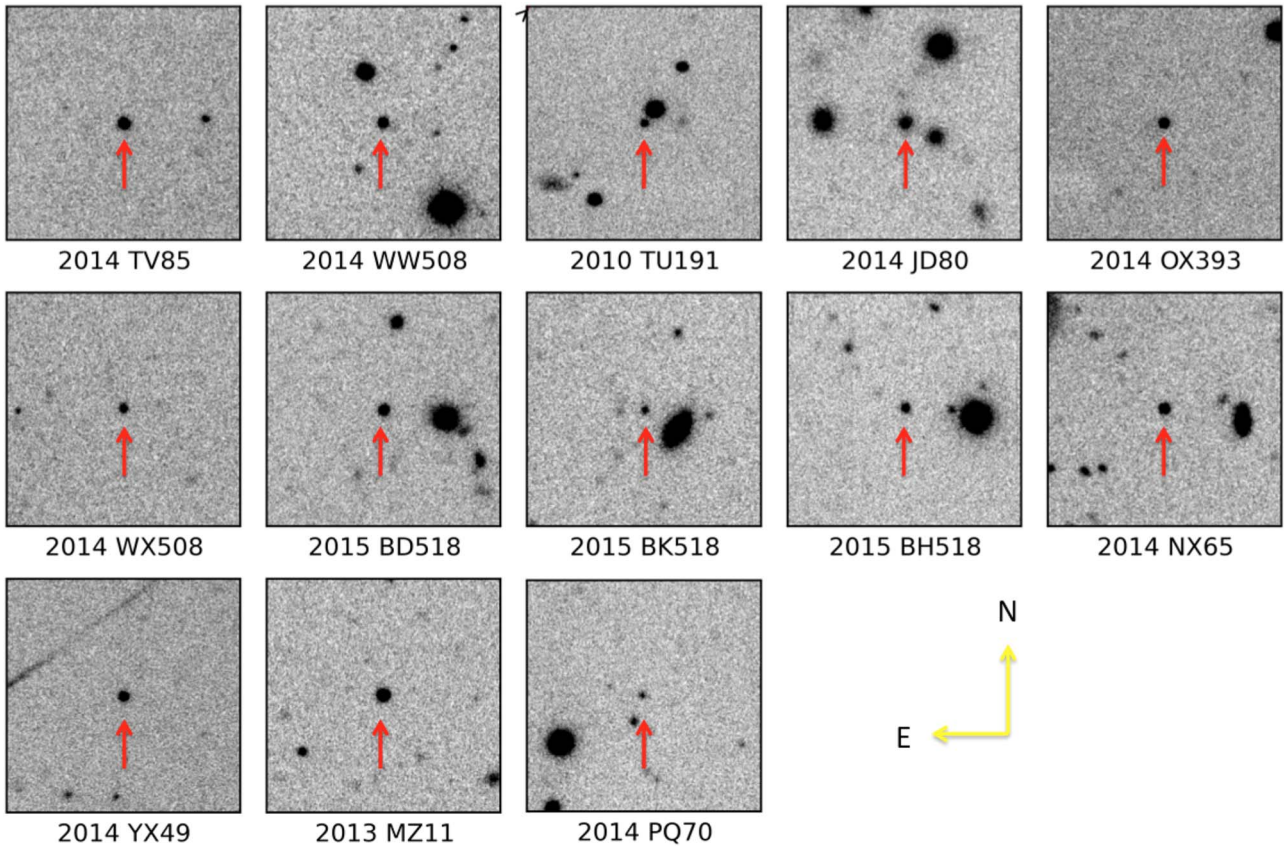

Figure 5. Postage stamp cutouts from stacked images of 13 Centaurs observed in this work. The spatial dimensions of each stamp are $30'' \times 30''$, and each stamp is centered on the object, with north up and east to the left. None of the objects showed obvious visual signs of activity, a conclusion supported by the SBP analysis (see Section 3.1).

Our DES search revealed numerous epochs of data for all but three of our targets (2010 TU_{191}, 2014 PQ_{70} and 2014 WX_{508}). DECam's archived multiextension FITS images have undergone basic reductions, including bias subtraction, flat-field correction, and fitting of a World Coordinate System as described in Morganson et al. (2018). We also applied our Python-based DECam image processing pipeline to individual images to (1) identify the FITS extension containing coverage of each target based on its JPL Horizons ephemeris coordinates, (2) save the identified individual CCD data and header metadata as a new FITS image file, (3) perform cosmic-ray removal utilizing the LACosmic technique (van Dokkum 2001) as implemented in ccdpro (Craig et al. 2017), and (4) perform photometric calibration based on Pan-STARRS field stars (Tonry et al. 2018).

3. Results and Discussion

3.1. Photometric Analysis and Nuclei Sizes

In order to search for activity in our observational data, we first identified the correct object in each star field by "blinking" the individual images and visually inspecting each one for extended surface brightness features moving along with the source. We then stacked the images using standard IRAF routines to increase the S/N. All our targets appeared stellar based on simple visual inspection, as can be seen in Figure 5.

To reveal activity much fainter than could be discerned by a visual inspection, we calculated surface brightness profiles (SBPs) of each target using the method of Meech et al. (1997) and compared it to the average SBPs of nearby stars. SBP analysis is a powerful method for detecting faint comae, and by averaging the mean brightness values within a fixed distance from the Centaur nucleus, we can increase our sensitivity to coma many-fold. Fortunately, our targets were at heliocentric distance large enough that their sky-plane motion was less than $0\farcs1$ minute^{-1}, and the trailing of the stars used in the SBP comparison was therefore negligible. In the most extreme case of the fastest-moving Centaur in our sample, 2014 NX_{65}, the tracking elongation was about 21% of the seeing FWHM values and hence undetectable. SBP analysis further revealed no evidence of low-level activity in any of the Centaurs in our sample (e.g., 2014 NX_{65}; Figure 6).

We calibrated our photometric data using sources from the GAIA (Gaia Collaboration et al. 2016) and ATLAS-REFCAT2 catalogs (Tonry et al. 2018) as photometric references and converted the apparent r'-band magnitudes, m_r, measured for our targets to absolute r'-band magnitudes, H_r (i.e., apparent magnitudes normalized to $r = \Delta = 1$ au and a solar phase angle of $\alpha = 0°$) using

$$H_r = H_r(\alpha) + 2.5\log[(1 - G_r) \cdot \Phi_1(\alpha) + G_r \cdot \Phi_2(\alpha)], \quad (2)$$

where the reduced magnitude, $H_r(\alpha)$, i.e., the apparent magnitude normalized to $r = \Delta = 1$ au, is given by

$$H_r(\alpha) = m_r(r, \Delta, \alpha) - 5\log(r\Delta), \quad (3)$$

where $m_r(r, \Delta, \alpha)$ is the apparent magnitude at a given heliocentric distance r, geocentric distance Δ, and phase angle

Table 3
Upper Limits on Sublimation and Dust Production Rates

Name	H_r[a]	R[b]	η[c]	$dim^{d}_{H_2O}/dt$	$dM^{e}_{CO_2}/dt$	dM^{f}_{CO}/dt	dM^{g}_{D}/dt	f_{Act}[h]	A_{Act}[i]	V_{AWI}[j]
2013 MZ_{11}	7.95	60.29	0.25	2.54×10^{-25}	1.74×10^{-2}	1.27×10^{7}	10.80	$8.50 \times 10 - 7$	3.88×10^{4}	27.14
2014 NX_{65}	9.27	32.91	0.05	9.84×10^{-24}	4.82×10^{-2}	3.57×10^{6}	0.76	$2.10 \times 10 - 7$	2.89×10^{3}	11.19
2014 TV_{85}	9.23	33.49	0.10	6.04×10^{-19}	9.77×10^{0}	5.23×10^{6}	2.14	$4.09 \times 10 - 7$	5.76×10^{3}	15.81
2015 BD_{518}	9.45	30.30	0.05	8.66×10^{-21}	1.24×10^{0}	4.34×10^{6}	0.74	$1.70 \times 10 - 7$	1.96×10^{3}	11.10
2015 BH_{518}	8.32	50.88	0.05	1.44×10^{-30}	4.69×10^{-5}	7.39×10^{6}	1.09	$1.48 \times 10 - 7$	4.81×10^{3}	12.65
2014 WW_{508}	10.48	18.82	0.05	4.49×10^{-18}	1.69×10^{1}	2.60×10^{6}	0.38	$1.47 \times 10 - 7$	6.53×10^{2}	8.90
2010 TU_{191}	10.75	16.61	0.05	3.81×10^{-20}	1.59×10^{0}	1.92×10^{6}	0.25	$1.32 \times 10 - 7$	4.57×10^{2}	7.77
2014 JD_{80}	8.68	43.20	0.05	7.76×10^{-25}	1.78×10^{-2}	5.02×10^{6}	1.17	$2.33 \times 10 - 7$	5.48×10^{3}	12.94
2014 OX_{393}	10.79	16.31	0.05	8.56×10^{-16}	1.78×10^{2}	2.34×10^{6}	0.36	1.53×10^{-7}	5.13×10^{2}	8.72
2014 YX_{49}	8.49	47.10	0.05	1.92×10^{-24}	3.34×10^{-2}	7.41×10^{6}	1.40	1.88×10^{-7}	5.26×10^{3}	13.72
2014 WX_{508}	10.68	17.15	0.05	2.60×10^{-17}	3.61×10^{1}	2.36×10^{6}	0.32	1.36×10^{-7}	5.02×10^{2}	8.40
2015 BK_{518}	14.16	3.46	0.10	3.15×10^{-10}	4.65×10^{3}	2.64×10^{5}	0.06	2.17×10^{-7}	3.27×10^{1}	4.73
2014 PQ_{70}	14.71	2.69	0.10	3.73×10^{-10}	5.51×10^{3}	3.13×10^{5}	0.04	1.21×10^{-7}	1.10×10^{1}	4.13

Notes.
[a] Absolute R-band total magnitude (at $R = \Delta = 1$ au and $\alpha = 0°$), using IAU H, G phase darkening, where $G = 0.13$ (Bauer et al. 2003).
[b] Effective nucleus radius, km.
[c] Coma limit parameter.
[d] Maximum H_2O sublimation rate, in kg s^{-1}.
[e] Maximum CO_2 sublimation rate, in kg s^{-1}.
[f] Maximum CO sublimation rate, in kg s^{-1}.
[g] CO-driven dust production rate, calculated assuming $f_{dg} = 6$, in kg s^{-1}.
[h] Effective active surface fraction of CO-driven activity.
[i] Effective active surface area of CO-driven activity, in m^2.
[j] Effective radius of a spherical AWI volume if solely sustaining upper limit on the CO gas flow, in m.

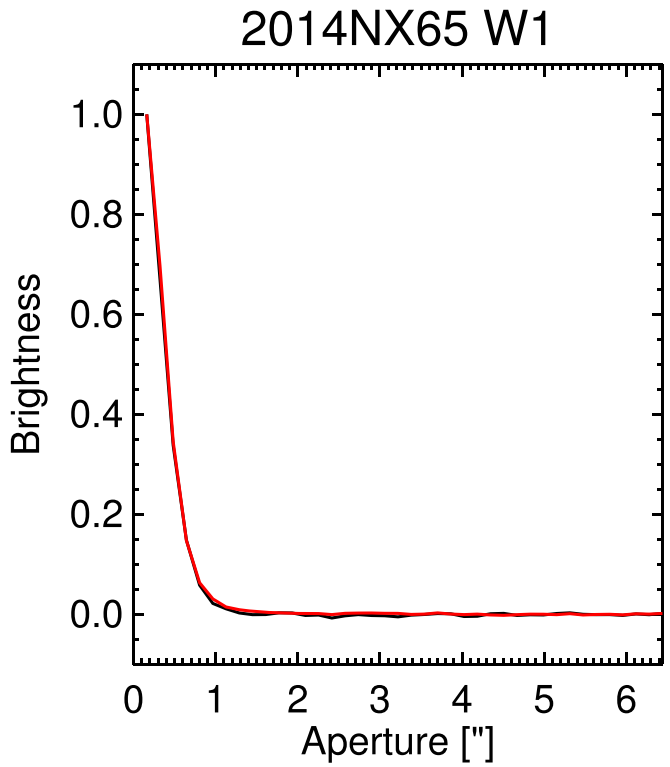

Figure 6. Radial SBP of 2014 NX_{65} (black line) compared to the average profile of background field stars (red line). Both profiles match almost exactly and therefore rule out faint activity of our target down to the surface brightness of 24.0 mag $arcsec^{-2}$.

α at the time of observation, with the average IAU slope parameter $G = 0.13 \pm 0.12$ measured in R-filter for Centaurs by Bauer et al. (2003). The Φ_i functions are given by

$$\Phi_i(\alpha) = \exp\left\{-A_i\left(\tan\frac{\alpha}{2}\right)^{B_i}\right\}, \quad (4)$$

where $A_1 = 3.33$, $A_2 = 1.87$, $B_1 = 0.63$, and $B_2 = 1.22$.

We then used our calculated absolute magnitudes and the average Centaur geometric albedo of $p = 0.08$ measured by Bauer et al. (2013) from the infrared WISE data to calculate effective nucleus diameters for our objects. The resulting values are summarized in Table 3. However, Centaurs are a unique small-body population given their striking color bimodality and a wide span of albedos (e.g., Peixinho et al. 2004, 2012), where the measured mean albedos for the two distinct Centaur groups are $6\% \pm 2\%$ for the blue group and $12\% \pm 5\%$ for the redder color group (Bauer et al. 2013). Therefore, if our targets belong to the blue group, they would be 15.4% larger on average, and if they are in the red group, they would be 18.4% smaller than if they had the mean albedo.

The photometric measurements reveal that our sample consists of an ensemble of average-sized Centaurs with effective radii of $2.7 \text{ km} < R < 60 \text{ km}$ if we use the mean albedo, where 2014 PQ_{70} is one of the smallest Centaurs ever observed with a mean nucleus radius of 2.7 km, similar to a typical JFC (Bauer et al. 2003; Fernández et al. 2013).

Table 4 summarizes the archival images from DECam that contain Centaurs in our sample and were suitable for photometric calibration, along with observing geometry parameters, filters used for the observations in question, and measured apparent photometric magnitudes. These images were taken for other research projects, and therefore they were taken using a variety of filters and exposure times. Out of 13, only 3 objects, 2015 PQ_{70}, 2010 TU_{191} and 2014 WX_{508}, were not present in the archive. For the rest of our targets, we have applied the SBP analysis following the procedure applied to the Gemini data, which revealed no

Table 4
DECam Archival Detections of Our Centaur Targets

Name	UT Date	UT Time	Filter	Δ[a]	r[b]	α[c]	Air Mass	m[d]
2013 MZ_{11}	2019-08-10	05:24:31.443	i'	18.891	19.874	0.732	1.04	20.87 ± 0.04
2013 MZ_{11}	2019-09-25	00:48:04.371	VR	18.976	19.826	1.572	1.15	21.38 ± 0.01
2014 JD_{80}	2015-08-16	02:54:48.666	VR	19.315	20.24	1.193	1.01	22.02 ± 0.13
2014 JD_{80}	2015-08-16	04:33:52.183	VR	19.316	20.24	1.196	1.03	22.05 ± 0.29
2014 JD_{80}	2015-09-05	23:47:24.726	VR	19.493	20.227	1.993	1.14	22.39 ± 0.10
2014 JD_{80}	2017-06-03	06:09:40.435	i'	19.311	19.854	2.509	1.26	22.52 ± 0.34
2014 JD_{80}	2017-07-02	07:23:43.929	g'	18.975	19.838	1.588	1.0	22.16 ± 0.32
2014 JD_{80}	2017-07-17	07:32:02.319	i'	18.878	19.83	1.058	1.05	21.56 ± 0.10
2014 JD_{80}	2017-08-27	02:08:09.002	r'	18.932	19.808	1.488	1.04	21.33 ± 0.14
2014 JD_{80}	2017-08-27	05:28:54.472	r'	18.933	19.808	1.493	1.13	21.01 ± 0.10
2014 JD_{80}	2017-08-28	01:49:49.905	r'	18.939	19.808	1.524	1.05	21.04 ± 0.13
2014 JD_{80}	2017-09-01	02:50:26.376	r'	18.97	19.806	1.673	1.0	21.65 ± 0.24
2014 JD_{80}	2017-09-01	03:51:49.346	r'	18.971	19.806	1.674	1.02	21.36 ± 0.20
2014 NX_{65}	2017-07-30	06:35:06.476	g'	17.94	18.65	2.275	1.12	23.34 ± 0.81
2014 NX_{65}	2017-07-30	06:36:37.613	g'	17.94	18.65	2.275	1.11	23.05 ± 0.32
2014 NX_{65}	2017-08-20	04:34:21.015	r'	17.751	18.656	1.43	1.19	22.41 ± 0.22
2014 NX_{65}	2018-08-12	05:09:17.383	r'	17.981	18.771	1.982	1.26	22.36 ± 0.50
2014 NX_{65}	2018-09-07	03:36:18.323	g'	17.814	18.78	0.902	1.22	23.58 ± 0.24
2014 NX_{65}	2018-09-12	03:13:44.044	r'	17.803	18.782	0.737	1.23	22.02 ± 0.16
2014 NX_{65}	2018-09-12	03:15:04.320	g'	17.803	18.782	0.737	1.22	23.17 ± 0.28
2014 NX_{65}	2019-09-26	05:30:12.957	VR	17.945	18.927	0.634	1.08	22.21 ± 0.03
2014 OX_{393}	2014-10-03	07:06:38.523	g'	11.047	12.032	0.863	1.34	23.04 ± 0.41
2014 OX_{393}	2014-10-03	07:08:36.795	r'	11.047	12.032	0.863	1.35	21.80 ± 0.11
2014 OX_{393}	2014-10-03	07:10:35.396	i'	11.047	12.032	0.863	1.36	21.87 ± 0.10
2014 OX_{393}	2015-11-02	02:53:11.989	r'	11.05	11.969	1.87	1.16	20.38 ± 0.16
2014 OX_{393}	2015-12-28	01:43:08.750	i'	11.764	11.974	4.637	1.4	21.50 ± 0.15
2014 OX_{393}	2015-12-28	03:00:59.051	i'	11.765	11.974	4.638	1.94	21.84 ± 0.15
2014 OX_{393}	2016-07-22	09:53:40.451	z'	12.005	12.022	4.848	1.29	21.77 ± 0.10
2014 OX_{393}	2016-07-22	10:10:05.819	z'	12.005	12.022	4.848	1.27	21.25 ± 0.10
2014 OX_{393}	2017-11-13	04:18:13.011	r'	11.337	12.306	0.963	1.39	21.80 ± 0.14
2014 TV_{85}	2015-03-09	04:16:42.821	VR	14.884	15.59	2.626	1.68	21.83 ± 0.06
2014 TV_{85}	2015-04-11	23:29:44.974	z'	15.345	15.562	3.627	1.31	21.41 ± 0.11
2014 TV_{85}	2016-01-10	05:46:06.736	r'	14.455	15.349	1.582	1.26	21.29 ± 0.08
2014 TV_{85}	2016-01-10	05:47:43.758	g'	14.455	15.349	1.582	1.26	21.75 ± 0.13
2014 TV_{85}	2017-03-01	00:50:23.512	r'	14.173	15.073	1.622	1.51	21.17 ± 0.08
2014 TV_{85}	2017-03-01	00:55:23.608	g'	14.173	15.073	1.622	1.49	21.63 ± 0.10
2014 TV_{85}	2018-01-28	06:50:34.844	z'	13.981	14.898	1.431	1.21	20.88 ± 0.06
2014 TV_{85}	2018-02-05	06:19:29.275	i'	13.943	14.894	1.037	1.21	20.69 ± 0.08
2014 TV_{85}	2018-12-13	06:21:48.624	g'	14.489	14.772	3.694	1.64	21.62 ± 0.11
2014 WW_{508}	2016-03-03	01:15:05.013	VR	13.159	13.47	4.051	1.49	21.10 ± 0.13
2014 WW_{508}	2019-02-28	02:32:20.617	VR	13.839	14.57	2.697	1.38	22.34 ± 0.15
2014 WW_{508}	2019-02-28	02:35:19.173	VR	13.839	14.57	2.697	1.39	22.55 ± 0.22
2014 YX_{49}	2016-12-29	06:27:42.080	g'	18.301	19.21	1.151	2.16	21.97 ± 0.11
2015 BD_{518}	2014-12-29	08:26:36.064	z'	15.716	16.466	2.264	1.73	21.62 ± 0.13
2015 BD_{518}	2015-04-12	00:52:43.348	r'	16.026	16.432	3.233	1.72	22.30 ± 0.14
2015 BD_{518}	2015-04-12	00:54:11.319	g'	16.026	16.432	3.234	1.72	22.48 ± 0.15
2015 BD_{518}	2016-01-15	06:58:55.054	r'	15.498	16.356	1.729	1.56	22.98 ± 0.25
2015 BD_{518}	2016-01-15	07:00:25.880	g'	15.498	16.356	1.729	1.56	23.12 ± 0.23
2015 BD_{518}	2017-01-11	05:59:11.086	z'	15.523	16.295	2.198	1.62	21.51 ± 0.06
2015 BD_{518}	2017-03-30	01:02:15.573	g'	15.539	16.287	2.381	1.57	22.01 ± 0.13
2015 BD_{518}	2018-02-12	05:36:58.517	g'	15.312	16.277	0.746	1.36	22.16 ± 0.07
2015 BH_{518}	2013-04-01	02:24:49.422	z'	24.537	25.345	1.351	1.14	19.46 ± 0.10
2015 BH_{518}	2014-03-28	00:03:22.996	VR	24.479	25.35	1.118	1.49	22.12 ± 0.11
2015 BH_{518}	2015-03-29	23:42:12.581	z'	24.478	25.36	1.077	1.63	22.38 ± 0.11
2015 BK_{518}	2017-03-02	05:30:37.098	g'	6.34	7.307	1.826	1.11	23.30 ± 0.24

Notes.
[a] Geocentric distance at the time of observation, au.
[b] Heliocentric distance at the time of observation, au.
[c] Phase angle at the time of observation.
[d] Apparent magnitude measured in given filter.

traces of a faint coma on the archival images similar to what we have observed with Gemini.

Three objects from our target list—2014 JD_{80}, 2014 NX_{65}, and 2013 MZ_{11}—were also observed with the Hubble Space Telescope (HST) by Li et al. (2020), who searched for activity among high-perihelion objects crossing the Centaur region. None of the HST targets have exhibited signs of activity.

3.2. Thermal Environment and Its Effect on Activity Levels

In our analysis of the thermal environment of the inspected Centaurs we were focusing on two possible activity sources: the solar-driven sublimation of surface volatiles, and the crystallization of AWI capable of releasing trapped gases. Multiple volatile species have been observationally detected in active Centaurs (e.g., Senay & Jewitt 1994; Womack & Stern 1997; Wierzchos et al. 2017; Womack et al. 2017), while there is no direct evidence of the presence of AWI (Lisse et al. 2013) on Centaur surfaces. It has to be noted that, due to their distance and their corresponding faintness, the detection of any volatile species on Centaurs sized similarly to our sample is extremely challenging (Kareta et al. 2021).

To assess the plausibility of activity driven by sublimation of surface volatile deposits, we have computed the theoretical maximal sublimation rates for the three most common volatiles found in comets, CO, CO_2, and H_2O, for each of our targets at their observed heliocentric distances. We used the thermal model described by Steckloff et al. (2015), which assumes a spherical graybody covered entirely in the pure volatile species of interest, with an albedo of approximately 4% and emissivity of 0.9. The model calculates the dynamic sublimation pressure and the sublimative mass-loss rate across the surface of a planetary body by numerically solving for the equilibrium temperature that balances incident solar energy with radiative and sublimative heat loss. The model integrates over the entire surface of the spherical nucleus and accounts for lower sunlight intensity toward the terminator due to increasing solar incidence angles, assuming that all sunlight is used to sublime volatiles. This model thus estimates maximal production rates capable from solar-driven activity.

Assuming comet-like dust-to-gas mass ratios f_{dg}, the calculated maximum sublimation rates can then be used to compute an idealized maximal dust production rate of the body under the assumption that the whole surface is active.

Our simplified modeled sublimation rates are summarized in Table 3 and assume only pure CO, CO_2, or H_2O surface ice as the major producer of gas molecules. Our results show that the CO sublimation rate is many orders of magnitude larger than CO_2 and H_2O sublimation rates for our targets at their respective heliocentric distances at the time of observation. CO thus has the strongest volatility in the region we are inspecting, and therefore we will consider it as the most likely sublimating ice species, and we will use it to constrain the active surface area and the dust production rates on our targets throughout the rest of this paper.

It is unrealistic to expect that CO or other supervolatiles would cover the whole surface at the analyzed heliocentric distances—we would observe strong surface CO-driven activity much farther away from the Sun because CO starts to sublimate at 25 K. It also has been shown (Wierzchos et al. 2017) that known Centaurs with detected CO emissions (with the one exception of 29P/Schwassmann-Wachmann 1 (29P); Womack et al. 2017) are actually significantly CO depleted compared to comet Hale-Bopp, which could be considered an unprocessed nucleus and had similar size and produced CO molecules at similar heliocentric distance. However, objects that may appear depleted in volatile species owing to the lack of detected activity could still retain sizable subsurface volatile deposits.

Idealized models of cometary nuclei depicting them as porous spheres composed of a mixture of dust and ices (Capria et al. 2000; Capria 2002) have shown that, in the cases of both pure CO ice and trapped CO gas, the source material for CO-driven activity is likely stored under the surface where the temperatures drop quickly, and in theory Centaurs should continuously release CO along their orbits owing to its low sublimation temperature and the shallow depth of the deposits (Mazzotta Epifani et al. 2006), which has not been observed. It is possible that during the residence in the Centaur region objects gradually undergo surface devolatilization and develop a dusty crust inhibiting the heat transfer and gas permeability of the upper layer, effectively reducing the sublimation rate and gas flow to the surface (Wierzchos et al. 2017). In the case of CO_2, most of the volume is likely stored just under the surface, but distant inactive Centaurs might have retained some surface patches of CO_2 since this supervolatile starts sublimating at $r \sim -15$ au (Steckloff et al. 2015; Meech et al. 2017). However, the CO_2 has not been detected on Centaur surfaces yet, because it is even more challenging than detecting CO with our current facilities, although it has been measured in situ on comets (A'Hearn et al. 2011).

Therefore, unless a Centaur is dynamically young in the region and still retains surface CO/CO_2 deposits, or has not developed a dust crust yet, we can expect the CO/CO_2 sublimation from the subsurface to be relatively weak and possibly go undetected until an external or internal force disturbs the volatile-rich layers.

If subsurface pockets of AWI are present, crystallizing, and releasing trapped volatiles to the surface, they could contribute to the gas flow from the subsurface. Laboratory experiments have shown that trapped gas could indeed be relatively abundant: AWI has the ability to retain gases up to a gas-to-ice-molecule ratio $f_{GI} = 3.3$ (Laufer et al. 1987). However, it should be noted that the crystallization of AWI is not capable of heating pockets of volatiles from below the surface because the phase transition cannot be both exothermic (releasing heat) and releasing trapped volatiles. Kouchi & Sirono (2001) showed that AWI absorbs heat when it crystallizes and releases trapped volatiles for concentrations of impurities (e.g., CO or CO_2 molecules) above 2%, which are typical in the interstellar dust and comets. The AWI phase transition itself therefore cannot produce enough heat to cause rapid sublimation of subsurface volatiles resulting in outburst, but it can act as a force opening the way to the surface and provide additional gas drag. For example, the well-known active Centaur 29P has been reported to have CO and dust outbursts that are not correlated and could be associated with multiple release mechanisms acting in parallel (Wierzchos & Womack 2020).

All above implies that the apparently inactive/dormant Centaurs orbiting within the AWI crystallization zone have probably already depleted their surface volatiles, since the average CO sublimation loss in the region is several meters per orbit (Li et al. 2020), and the CO_2-driven activity would be visible, but they could still contain subsurface pockets of volatiles and AWI buried under the dust crust. A sudden rapid orbital change pushing the perihelion closer to the Sun could jump-start the crystallization front, which will move rapidly

releasing trapped gas until enough pressure builds up to cause a landslide or opens a sinkhole exposing subsurface layers. This process could lead to large-scale outgassing and/or outburst, possibly with a significant lag, as was observed in several active Centaurs (Mazzotta Epifani et al. 2006) and also in quasi-Hilda P/2010 H2 (Vales) (Jewitt & Kim 2020). Such rapid release of gases could also eject a large boulder or a chunk of the parent body that can continue to disintegrate, as has been likely observed during a dramatic outburst of 174P/Echeclus in 2005, where the the nucleus and coma brightness peaks were spatially separated (Bauer et al. 2008; Rousselot 2008; Kareta et al. 2019). As the crystallization front moves through the body, it could keep building the pressure pockets and create openings throughout the surface even far away from perihelion, and in subsequent orbital passages until the volatile deposits in each pocket are depleted.

However, crystallization cannot be sustained for a time longer than 10^4–10^5 yr (Guilbert-Lepoutre 2012), further suggesting that active Centaurs have young orbits and have only recently been scattered inside to the warmer regions of the solar system.

Using 174P/Echeclus as an example, we can calculate the volume of AWI necessary to release the observed dust volume. Given the dust production rate observed during the 2005 outburst (400 kg s^{-1}; Bauer et al. 2008), f_{GI} for AWI, the density of water ice ($\rho_{H_2O} = 1000$ kg m^{-3}), and the range of dust-to-gas ratios measured for comets and estimated for active Centaur 29P ($f_{dg} = 1$–8; Y. Fernández, personal communication; Fernández et al. 2020; Wierzchos & Womack 2020), it would require between ~15 and 120 kg of AWI to crystallize every second and release trapped CO to match the observed dust production if AWI is the single source. A ~1-month-long outburst would require between 10^7 and 10^8 kg of amorphous ice, or a sphere of ~20–40 m in diameter, which is an AWI pocket similar in size to what Jewitt & Kim (2020) calculated for a Hilda asteroid undergoing an outburst of similar magnitude.

It should be noted that our calculated values should only be used as order-of-magnitude estimates given that there are no direct simultaneous measurements of gas and dust mass loss from an active Centaur. The f_{dg} ratio can change depending on the Centaur and whether the mass loss is a product of a quiescent activity or an outburst (Fernández et al. 2020). A fresh sinkhole opening up and causing an outburst could be much dustier than a steady-state outgassing event diffusing through surface regolith. For example, Wierzchos & Womack (2020) has shown that in the case of 29P several CO outbursts did not have a corresponding dust outburst. There is currently a real lack of knowledge of the gas-to-dust ratio of Centaurs owing to observational limitations, which will be hopefully addressed and alleviated with future works using JWST (Kelley et al. 2016), but such rigorous analysis is beyond the scope of this paper.

3.3. Mass-loss Rates and Fractional Active Surface Area

We used the maximum CO sublimation production rates from our thermodynamical model to derive the maximum surface sublimation-driven dust production rate, dM_{CO}/dt, assuming CO to be the most likely volatile to drive the activity at heliocentric distances of our targets, and $f_{dg} = 1$ estimated for Centaur 29P during its quiescent activity phase (Fernández et al. 2020; Wierzchos & Womack 2020). This value most likely represents the volume of dust expected to be lofted by steadily escaping gas from a weakly active Centaur such as the targets of this study. The in situ f_{dg} measurements on 67P revealed the ratio to be much higher closer to the nucleus, $f_{dg} = 4 \pm 2$, compared to ratios $f_{dg} = 0.1$–2.0 typically measured remotely for comets (e.g., Weiler et al. 2003; Choukroun et al. 2020), but the comet had an active water-ice sublimation and was near its perihelion at the time the measurements were taken; thus, it could be expected that the volume of dust being lofted was higher than in our targets.

Then, using the synthetic coma limit technique following Luu & Jewitt (1992), we calculated the observed effective upper limit on the dust production rate. To find quantitative limits on weak activity, we compared every Centaur's point-spread function (PSF) with seeing-convolved models of weak comae. With the same image scale and PSF as our data, models and data can be directly compared in order to ascertain activity levels. We first created model point sources and then generated a series of synthetic PSFs with varying coma levels and convolved these with the seeing (Figure 7). Coma levels were parameterized by $\eta = C_c / C_n$, where C_c and C_n are the scattering cross sections of the coma and nucleus, respectively, and the reference photometry aperture radius used was $\Phi = 4\farcs04$. For our analyses, we used coma levels of $\eta = 0.00$–0.25 in $\eta = 0.05$ increments.

Increasing coma levels generated this way generally has little effect on the profile cores but does broaden the profile wings. We then noted at which coma level were the synthetic profiles most similar to the profile of the target object. Our comparison of the coma models to measured profiles of our sample Centaurs produced no indication of activity within our detection limits. However, we used the resulting limiting coma parameter η_{lim} to convert to the observed effective upper limit on the dust production rate dM_D/dt via

$$dM_D/dt = \frac{(1.1 \times 10^{-3}) \cdot \pi \rho \bar{a} \eta_{lim} R^2}{\Phi r^{0.5} \Delta}, \quad (5)$$

where $\rho = 2500$ kg m^{-3} is the assumed grain density consistent with carbonaceous chondrites, which are associated with primitive C-type objects and are most likely the closest match to the Centaurs (Britt et al. 2002), $\bar{a} = 0.5 \times 10^{-6}$ m is the assumed weighted mean grain radius (Bauer et al. 2008), R is the object's effective radius, Φ is the angular photometry radius in arcseconds, r is the heliocentric distance in astronomical units, and Δ is the geocentric distance in astronomical units (Luu & Jewitt 1992).

By comparing the maximal production rates of CO and CO_2 derived from the surface sublimative mass loss and the upper limit on dust production rates derived from our observations, we can calculate the effective fraction of active surface area of the particular Centaur at the time of the observation and the actual active area as a function of the object's diameter. Since we are using a photometric method to derive the upper limits on dust production, the possible changes in dust-to-gas ratio affect the size of the effective fraction of the active surface area —the active area scales with $1/f_{dg}$, because a larger active area is needed to lift the same amount of dust grains at fixed gas flow, if the f_{dg} is smaller. The resulting production rates are on order of several kilograms, with the effective active surface areas for each target ranging from several to several thousand square meters in the case of CO-driven activity. Our values are 1–2 orders of magnitude smaller than values calculated for

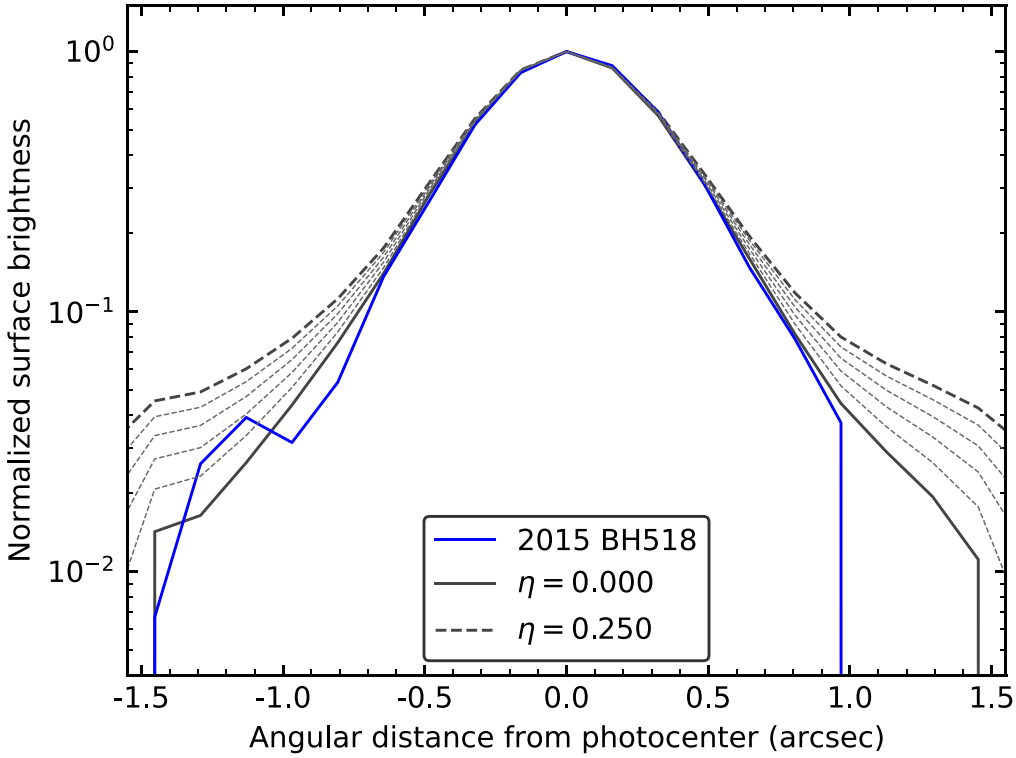

Figure 7. Comparison of the PSF for object 2015 BH_{518} with a series of synthetic PSFs with varying coma levels η. The coma parameter for this object was 0.05.

other weakly active Centaurs (e.g., Bauer et al. 2003; Mazzotta Epifani et al. 2014, 2017). Since the gas production rates from a CO_2-driven activity are several orders of magnitude lower than those calculated for CO and are strongly dependent on the heliocentric distance, the active surface areas constrained by our coma limit technique would be unrealistically large for our most distant targets. However, patches only several hundred square meters of sublimating surface CO_2 would sustain the observed dust production limits on two of our closest targets—2014 PQ_{70} and 2015 BK_{518}.

If this mass-loss volume is to be attributed to an escaped gas from AWI crystallization, it would require a relatively modest subsurface pocket akin to a sphere with several-meter radius, which is in agreement with AWI pocket sizes estimated for outbursting quasi-Hilda P/2010 H2 (Vales) (Jewitt & Kim 2020). Resulting values are summarized in Table 3.

Our dust production upper limits can be well explained by a combined gas drag from volatiles released from crystallized AWI and from sublimating ice patches under the surface exposed to the Sun by the pressure of escaping molecules.

Cometary nucleus models (e.g., Prialnik & Podolak 1995; Capria et al. 2000) predict that CO molecules should percolate through the outer layers of the body and flow uniformly from anywhere on the surface on both the nightside and dayside. This indicates that there should also be a uniform associated dust release due to the gas drag, unlike the dust mass loss caused by water sublimation, which tends to be released only from the dayside. Also, it has been proposed that sublimation of CO and CO_2 and the associated dust production rate change very slowly with time after the activity onset because it originates in the subsurface layers (Capria et al. 2000; Capria 2002). This would mean that if there are large enough subsurface CO deposits on Centaurs, most of the dynamically younger population members should exhibit a low-scale outgassing and dust mass loss along their orbits similar to what has been observed in (2060) 95P/Chiron, which would be in most cases fainter than our detection limits (e.g., Kareta et al. 2021).

3.4. Orbital Evolution

To track past orbital evolution and identify any recent potential activity-triggering events such as significant orbital changes or close encounters with giant planets, we ran several sets of backward numerical integrations for each of our targets. We used the Bulrisch–Stöer integrator in the Mercury6 *N*-body integration package (Chambers & Migliorini 1997), which is capable of handling close planetary encounters with minimal loss of precision by using an adaptive time step once an object crosses a massive body's Hill sphere. All integrations used a 30-day time step, which is an sufficiently precise to map the evolution of orbits with decades-long periods typical for Centaurs. Particles were removed from the integrations when they collided with the Sun or a planet, or reached semimajor axes of $a > 100$ au and were considered to be ejected from the solar system. Dynamical clones were generated for each object using covariance matrices from the JPL Small Body Database.[10] All of our targets have well-defined orbits with up to 10 opposition arcs and low residuals resulting in small dispersion of clones from the nominal orbit.

For our first set of integrations, we produced 50 clones for each object and ran them as massless particles under the gravitational influence of eight planets and the Sun for 100,000 yr into the past, which is the the upper time limit on AWI survival on Centaurs (Guilbert-Lepoutre 2012). The orbits in the Centaur region are subjected to strong gravitational influence from giant planets, and their orbital dynamics becomes chaotic very quickly. Therefore, it

[10] https://ssd.jpl.nasa.gov/sbdb.cgi

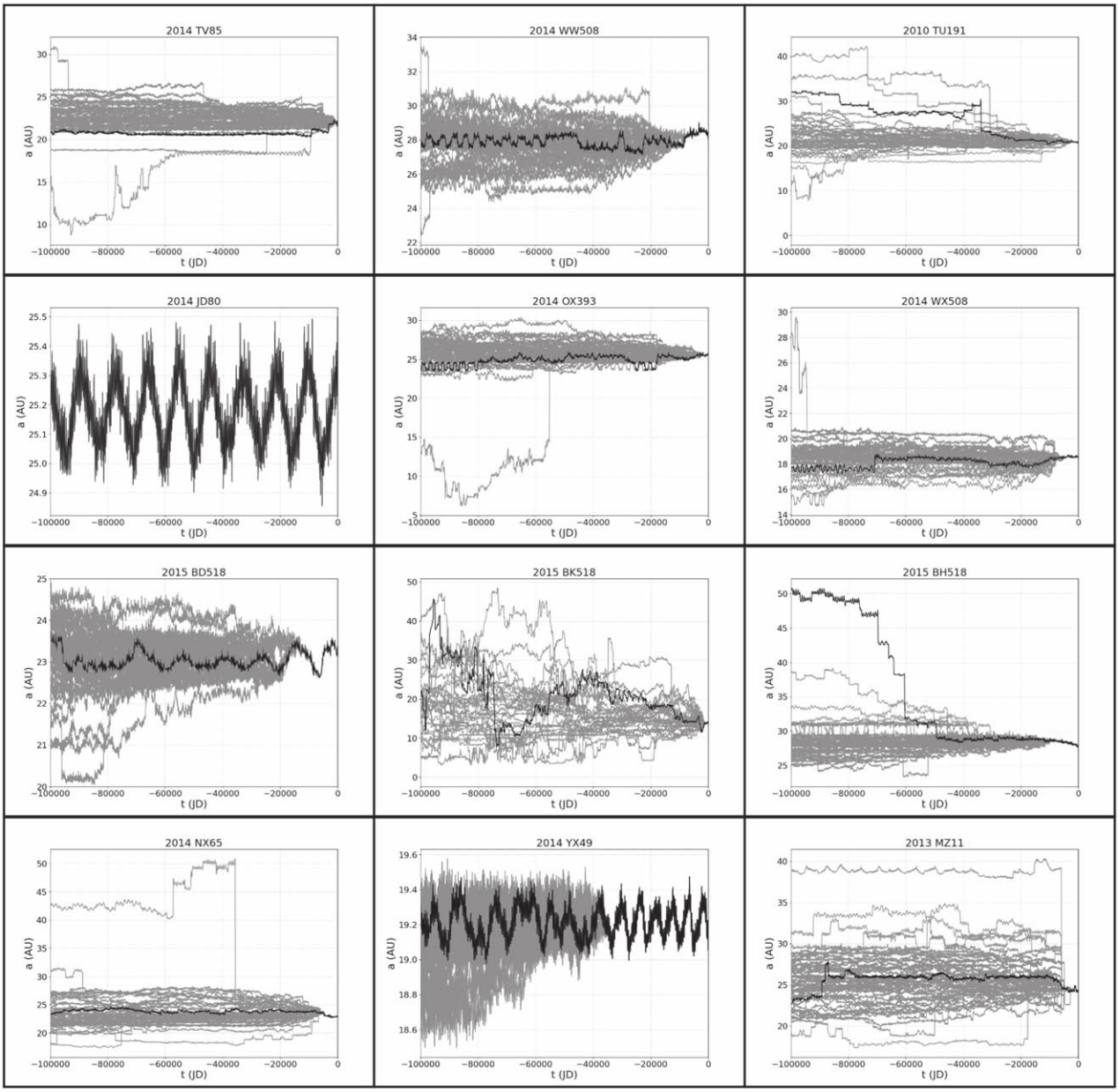

Figure 8. Evolution of semimajor axis of 12 Centaurs over the past 100,000 yr.

is nearly impossible to know the system's dynamical evolution past the point in the history where the clones start to diverge (Morbidelli et al. 2020).

After examination of these long-term integrations, we ran two more sets of integrations: (a) using a time step of 10 days for the past 5000 yr in order to investigate clone evolution before the individual orbits started to diverge, and (b) using a 1-day time step for 200 yr into the past to search for extremely recent orbit changes similar to other Centaurs observed in outburst (e.g., Fernández et al. 2018).

Our analysis of the orbital histories revealed that most of the Centaurs in our sample have relatively stable orbits with only minor orbital changes as can be seen in Figures 8–11. Our 100 kyr integrations show that the nominal orbit of each target and those of their clones start to diverge on $\sim 10^3$ yr timescales, where the chaotic environment makes any determination of the evolution before this point statistical only. Such a point of divergence is typically associated with a close encounter with a planet.

We can divide the observed orbital behavior of our targets and their expected activity levels into three groups based on perihelion distance:

1. $q \gtrsim 15$ au: Objects with perihelia outside of the AWI crystallization zone (and CO_2 sublimation limit) tend to have stable orbits on the considered timescale, with changes in perihelion and semimajor axis of Δa, $\Delta q \lesssim$ 1–3 au. Objects 2015 TV_{85}, 2014 JD_{80}, 2015 BH_{518}, 2015 BD_{518}, 2014 NX_{65}, 2013 MZ_{11}, and most clones of 2010 TU_{191} fall within this group. We expect very limited activity driven by surface or subsurface volatiles owing to fairly long residence inside Neptune's orbit and therefore the depletion of surface sources, and we do not expect significant crystallization of AWI at the distances they reside in.

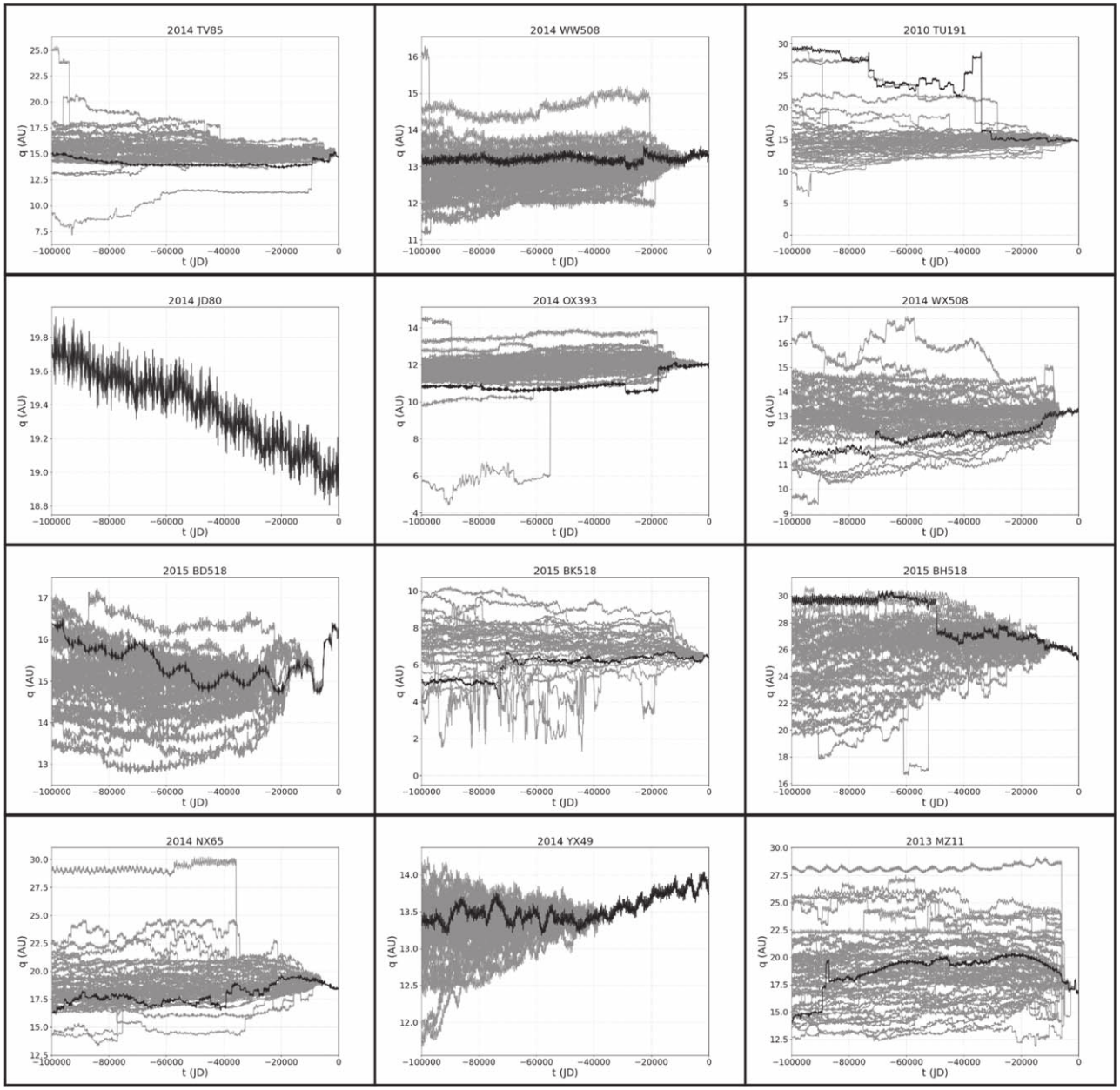

Figure 9. Evolution of perihelion distance of 12 Centaurs over the past 100,000 yr.

2. 7 au $\lesssim$ q $\lesssim$ 15 au: Objects with perihelion distances in the AWI crystallization zone. Centaurs 2014 YX_{49}, 2010 OX_{393}, 2014 WX_{508}, and 2014 WW_{508} belong to this group, and it is entirely possible that the AWI crystallization/CO_2 has been underway, but the released gases remain under the surface or remain below our detection limit. However, objects in this group experienced only minor orbital changes in the past 10^5 yr, and we would expect only minimal gas and dust loss driven by the crystallization since the front should have stopped propagating inside the bodies or has propagated too deep into the nucleus over the residence time in the zone (Guilbert-Lepoutre 2012). As we noted before, temperatures in this region are too high for any supervolatiles to have survived on the surface until present day.
3. $q \lesssim 7$ au: There are two Centaurs in our sample with perihelia and semimajor axes below 7 au: 2015 BK_{518} and 2014 PQ_{70}. Both have current $T_J > 3$ and $T_S < 3$, and their orbital evolution can be traced with a reasonable precision $\sim$2000 yr into the past, where the orbits of clones start to turn chaotic under the strong gravitational influence from Saturn. Our integrations show wide diffusion of possible semimajor axes, while the perihelia changed very little from the current value, similarly to what other works have found on the evolution of low-perihelion Centaurs (Fernández et al. 2018; Kareta et al. 2019; Steckloff et al. 2020). It is possible that Centaurs in this group experienced periods of activity in the past, given their proximity to the Sun, with surface volatiles completely depleted and perhaps some remaining pockets of subsurface ices still isolated under the surface. If they entered the AWI crystallization zone within the past $\sim 10^5$ yr, the AWI crystallization front might be propagating under the surface and, with favorable

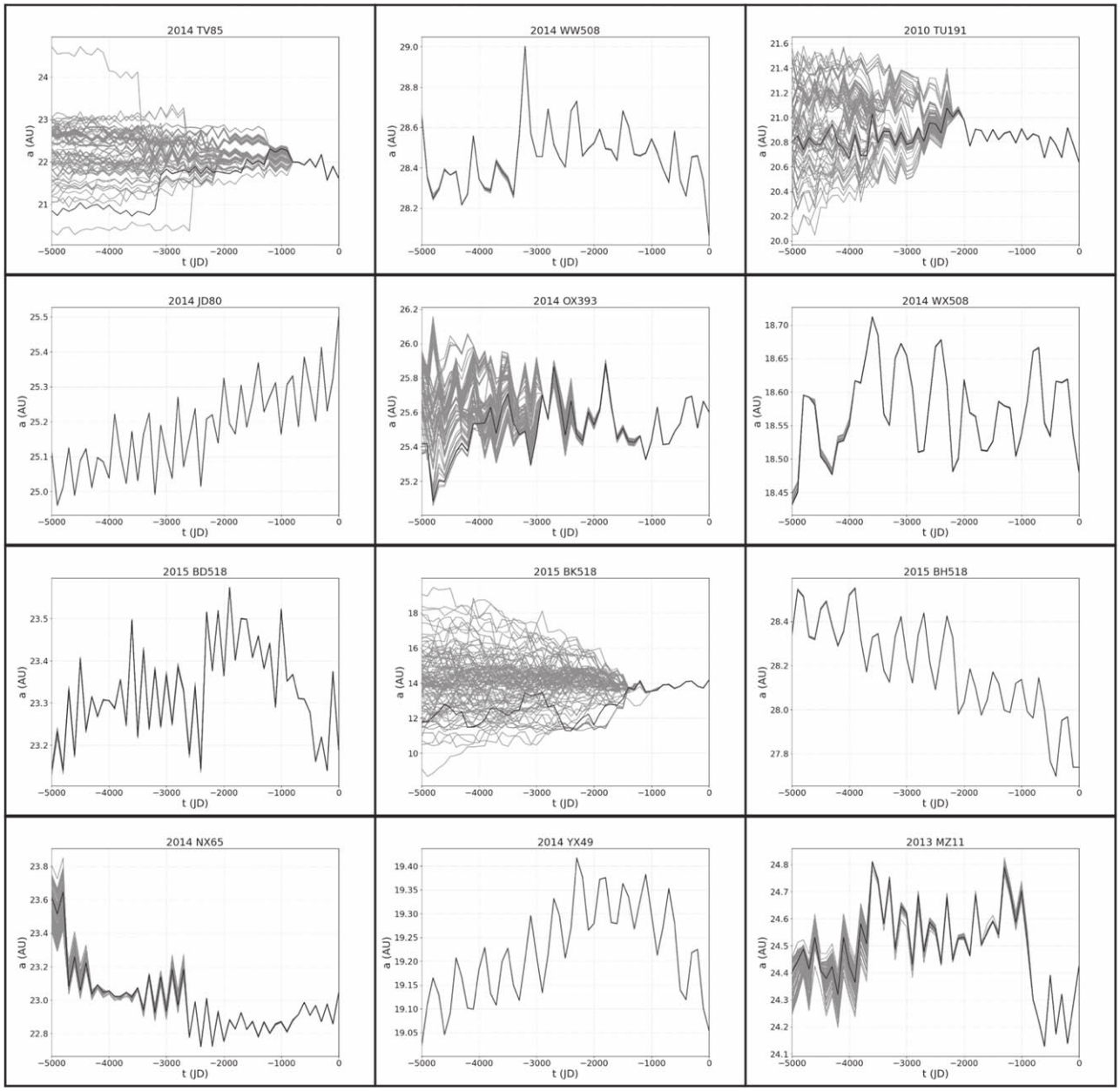

Figure 10. Evolution of semimajor axis of 12 Centaurs over the past 5000 yr.

conditions, can become active again. For example, 2014 PQ_{70} in particular would be a good candidate for an outburst monitoring campaign because it has experienced a decrease in semimajor axis ∼70 yr ago (Figures 12 and 13) similar to what has been observed in other active Centaurs (Mazzotta Epifani et al. 2006), and we could witness yet another bout of activity triggered by this event in the coming years.

There are three other notable Centaurs in our sample. 2010 TU_{191} may be a fairly new addition to the Centaur region. Figure 10 shows that three of the clones including the nominal orbit experienced a close encounter with Neptune within 0.03 au ∼38,000 yr ago, reducing the perihelion distance by 15 au within a decade and illustrating some drastic orbital changes that are common in the Centaur region. This object could represent a "fresh" Centaur with high likelihood of undisturbed surface volatile deposits, and it is entirely possible that it is weakly active below our detection limits and might become increasingly more active in the future.

Meanwhile, 2014 JD_{80} is in a 3:2 mean-motion resonance with Uranus, and additional 0.5 Myr integration suggests that it will stay resonant for the next ∼1 Myr (K. Volk, personal communication).

Lastly, an apparently inactive object (2014 OX_{393}) that we observed in this work has a very similar ratio of perihelion distance and heliocentric distance at the time of observation and orbital elements to two known active Centaurs—167P/CINEOS (248835) and 2006 SX_{368} (Jewitt 2009, 2015)—at the times of their outbursts (Figure 1), which could indicate that 2014 OX_{393}'s inactivity could be due to having a different orbital history compared to the other two. While 2014 OX_{393} has a stable orbit just inside the upper limit of the crystallization zone, either it lacked an activity trigger in the form of a sudden perihelion drop and rapid warming of the surface, or the past activity has depleted surface volatiles.

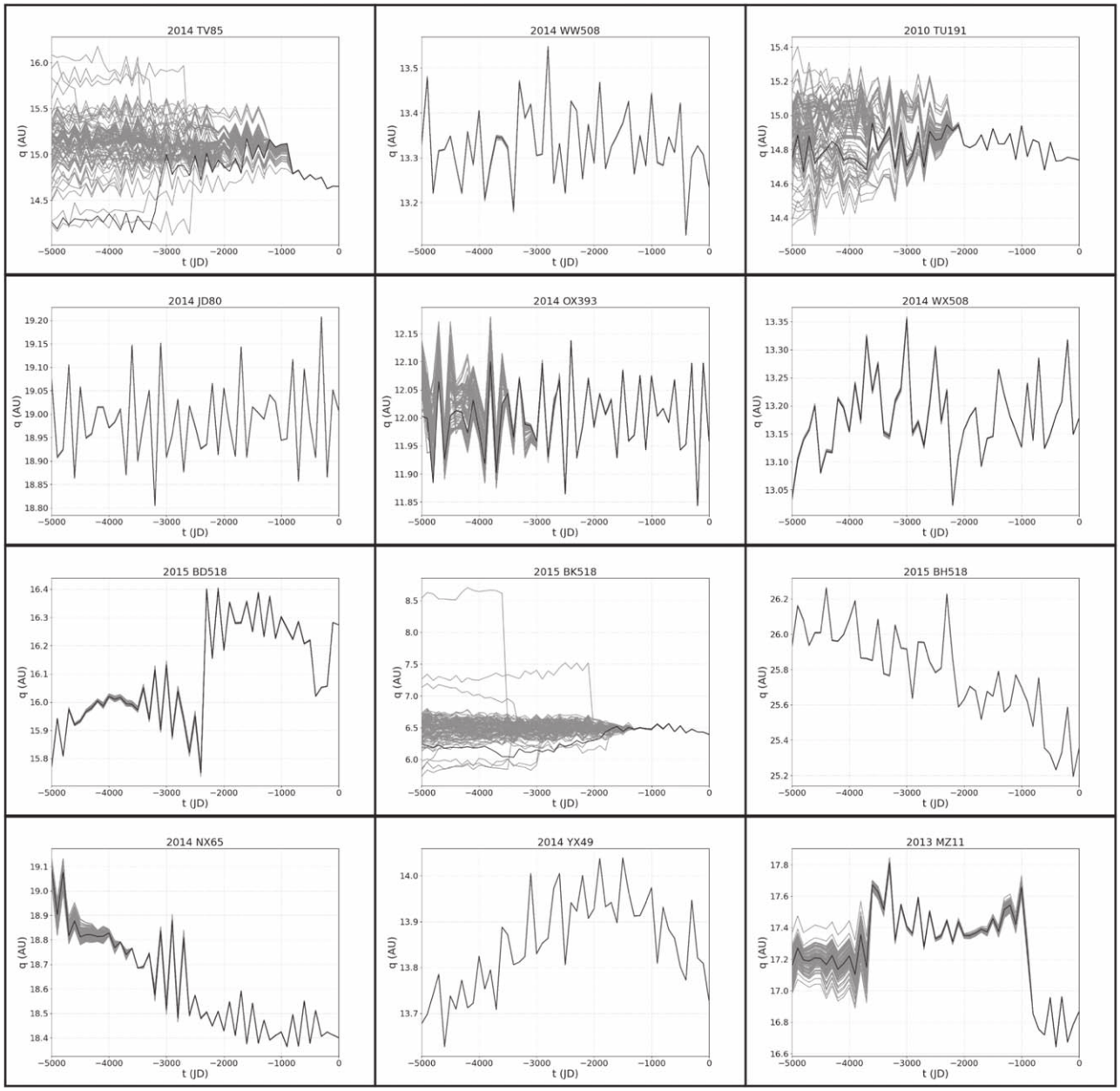

Figure 11. Evolution of perihelion distance of 12 Centaurs over the past 5000 yr.

With one exception, our fully inactive Centaur sample has had relatively stable orbits, adding support to the idea that sudden orbital changes might trigger or restart activity in the Centaurs.

4. Conclusions

We have observed 13 Centaurs with the Gemini North telescope with the goal of searching for comet-like activity beyond the orbit of Jupiter. Our targets were selected from objects newly discovered in the Pan-STARRS1 detection database and thus have orbital arcs covering up to a decade. Most objects in our sample have orbits crossing the range of heliocentric distances where the temperatures allow for crystallization of AWI, speculated to be the major activity driver in Centaurs. We conclude the following:

1. None of the Centaurs in our sample showed signs of activity either in our observations with Gemini or in archival images from DECam dating back to 2013. However, we cannot rule out the presence of faint comae below our detection limits.
2. The thermodynamical model we used allowed us to calculate the theoretical maximal sublimation rate of the three most common volatile species found on comets—CO, CO_2, and H_2O, and our results suggest that the majority of sublimation-driven activity at the analyzed heliocentric distances should be due to CO. Due to the heliocentric distances and orbital histories of investigated Centaurs, it is unlikely that free CO or CO_2 remains on the surfaces, but it is possible our targets retain subsurface volatile deposits, and some of them could exhibit low-level gas and dust mass loss below our detection limits.

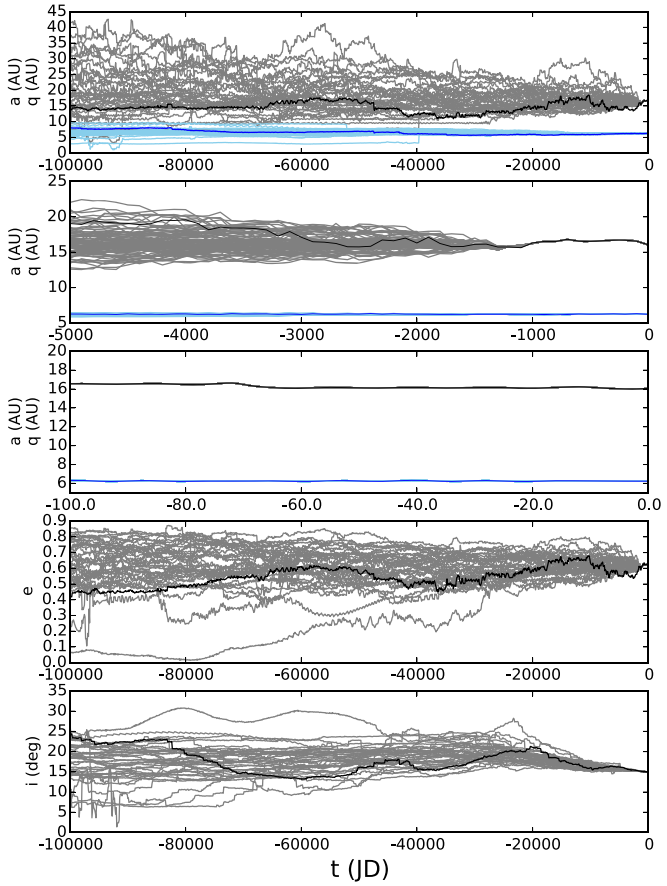

Figure 12. Orbital evolution of low-perihelion Centaur 2014 PQ_{70}. The three uppermost panels show the orbital evolution of semimajor axis (black line) and perihelion distance (blue line) for 100 kyr, 5 kyr, and 200 yr into the past (top to bottom). The two lowermost panels show the evolution of eccentricity and the orbital inclination in the past 100 kyr.

3. The upper limit on dust production rates and fractional active surface areas resulting from our coma modeling based on the nondetection of activity and the maximum surface sublimation rates are in agreement with rates estimated independently for other inactive Centaurs (e.g., Bauer et al. 2003; Jewitt 2009; Li et al. 2020). If there are no surface supervolatiles present and sublimating, the estimated dust gas production rates could be sustained by a modestly sized (volume on order of several square meters) exposed pockets of AWI crystallizing and releasing trapped gas molecules.
4. Our orbital history analysis revealed that most of our targets have relatively stable orbits with no significant recent changes in perihelion distance. Our results are consistent with earlier work suggesting that the activity on Centaurs is most likely triggered by sudden drops in perihelion distance and/or semimajor axis induced by close encounters with giant planets, which change the thermal balance in the body. The rapid warming and crystallization of AWI can then release trapped gas and build up pressure under the surface, which leads to exposure of more volatile material and subsequent outbursts.
5. Our numerical integrations show that Centaur 2014 PQ_{70} has experienced a drop in semimajor axis larger than 0.5 au about 50 yr ago, similar to what has been seen in other active Centaurs in the past, and is therefore a good candidate for monitoring of possible future outbursts of activity.

This work was supported by NSF AST grant No. 1910275.

We thank Kat Volk for helpful insights into Centaur dynamics and Yan Fernández for insights into the dust-to-gas ratio of 29P.

The authors recognize and acknowledge the very significant cultural role and reverence that the summit of Maunakea has always had within the indigenous Hawaiian community. We are most fortunate to have the opportunity to conduct observations from this mountain.

This project used public archival data from the Dark Energy Survey (DES). Funding for the DES Projects has been provided by the U.S. Department of Energy, the U.S. National Science Foundation, the Ministry of Science and Education of Spain, the Science and Technology Facilities Council of the United Kingdom, the Higher Education Funding Council for England, the National Center for Supercomputing Applications at the University of Illinois at Urbana-Champaign, the Kavli Institute of Cosmological Physics at the University of Chicago, the Center for Cosmology and Astro-Particle Physics at The Ohio State University, the Mitchell Institute for Fundamental Physics and Astronomy at Texas A&M University, Financiadora de Estudos e Projetos, Fundação Carlos Chagas Filho de Amparo à Pesquisa do Estado do Rio de Janeiro, Conselho Nacional de Desenvolvimento Científico e Tecnológico and the Ministério da Ciência, Tecnologia e Inovação, the Deutsche Forschungsgemeinschaft, and the Collaborating Institutions in the Dark Energy Survey. The Collaborating Institutions are Argonne National Laboratory, the University of California at Santa Cruz, the University of Cambridge, Centro de Investigaciones Energéticas, Medioambientales y Tecnológicas-Madrid, the University of Chicago, University College London, the DES-Brazil Consortium, the University of Edinburgh, the Eidgenössische Technische Hochschule (ETH) Zürich, Fermi National Accelerator Laboratory, the University of Illinois at Urbana-Champaign, the Institut de Ciències de l'Espai (IEEC/CSIC), the Institut de Física d'Altes Energies, Lawrence Berkeley National Laboratory, the Ludwig-Maximilians Universität München and the associated Excellence Cluster Universe, the University of Michigan, the National Optical Astronomy Observatory, the University of Nottingham, The Ohio State University, the OzDES Membership Consortium, the University of Pennsylvania, the University of Portsmouth, SLAC National Accelerator Laboratory, Stanford University, the University of Sussex, and Texas A&M University.

Based in part on observations at Cerro Tololo Inter-American Observatory, National Optical Astronomy Observatory, which is operated by the Association of Universities for Research in Astronomy (AURA) under a cooperative agreement with the National Science Foundation.

This research has made use of data and/or services provided by the International Astronomical Union's Minor Planet Center.

This work has made use of data from the European Space Agency (ESA) mission Gaia (https://www.cosmos.esa.int/gaia), processed by the Gaia Data Processing and Analysis Consortium (DPAC, https://www.cosmos.esa.int/web/gaia/dpac/consortium). Funding for the DPAC has been provided by national institutions, in particular the institutions participating in the Gaia Multilateral Agreement. Eva Lilly would like to thank her children Betty and Sammy for being excellent

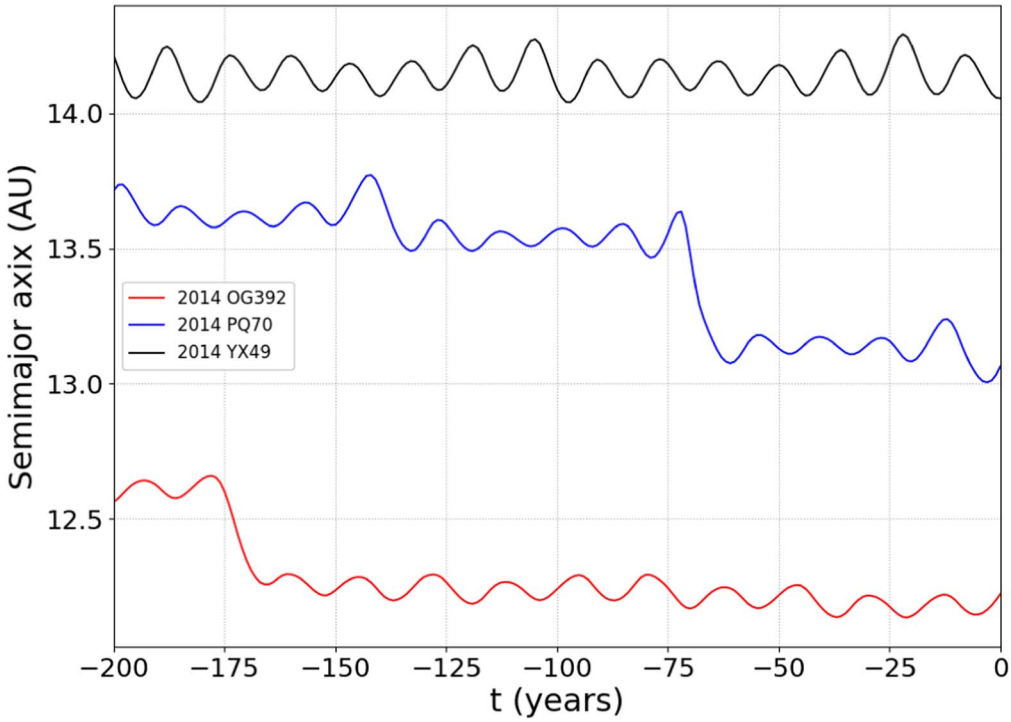

Figure 13. Evolution of semimajor axis of the recently discovered active Centaur 2014 OG_{392} and two apparently inactive Centaurs observed in this work. Centaur 2014 PQ_{70} has experienced a decrease in semimajor axis of similar amplitude to 2014 OG_{392} The semimajor axes of 2014 PQ_{70} and 2014 YX_{49} have been scaled down by 5 and 3 au, respectively, for better comparison on the plot.

nappers so this paper could be written, and she wishes to express her gratitude to PSI for having an excellent support system for families with children.

ORCID iDs

Eva Lilly https://orcid.org/0000-0002-7696-0302
Henry Hsieh https://orcid.org/0000-0001-7225-9271
James Bauer https://orcid.org/0000-0001-9542-0953
Jordan Steckloff https://orcid.org/0000-0002-1717-2226
Robert Weryk https://orcid.org/0000-0002-0439-9341
Richard J. Wainscoat https://orcid.org/0000-0002-1341-0952
Charles Schambeau https://orcid.org/0000-0003-1800-8521

References

Abbott, T. M. C., Abdalla, F. B., Allam, S., et al. 2018, ApJS, 239, 18
A'Hearn, M. F., Belton, M. J. S., Delamere, W. A., et al. 2011, Sci, 332, 1396
Astropy Collaboration, Price-Whelan, A. M., Sipőcz, B. M., et al. 2018, AJ, 156, 123
Bauer, J. M., Choi, Y.-J., Weissman, P. R., et al. 2008, PASP, 120, 393
Bauer, J. M., Fernández, Y. R., & Meech, K. J. 2003, PASP, 115, 981
Bauer, J. M., Grav, T., Blauvelt, E., et al. 2013, ApJ, 773, 22
Bockelée-Morvan, D., Crovisier, J., Mumma, M. J., & Weaver, H. A. 2004, in Comets II, ed. M. C. Festou, H. U. Keller, & H. A. Weaver (Tucson, AZ: Univ. Arizona Press), 391
Britt, D. T., Yeomans, D., Housen, K., & Consolmagno, G. 2002, in Asteroids III, ed. W. F. Bottke, Jr. et al. (Tucson, AZ: Univ. Arizona Press), 485
Cabral, N., Guilbert-Lepoutre, A., Fraser, W. C., et al. 2019, A&A, 621, A102
Capria, M. T. 2002, EM&P, 89, 161
Capria, M. T., Coradini, A., De Sanctis, M. C., & Orosei, R. 2000, A&A, 357, 359
Chambers, J.-E., & Migliorini, F. 1997, BAAS, 29, 1024
Chandler, C. O., Kueny, J. K., Trujillo, C. A., Trilling, D. E., & Oldroyd, W. J. 2020, ApJL, 892, L38
Choi, Y.-J., Weissman, P., Chesley, S., et al. 2006, CBET, 563, 1
Choukroun, M., Altwegg, K., Kührt, E., et al. 2020, SSRv, 216, 44
Craig, M., Crawford, S., Seifert, M., et al. 2017, astropy/ccdproc:v1.3.0.post1
Di Sisto, R. P., & Brunini, A. 2007, Icar, 190, 224
Durda, D. D., & Stern, S. A. 2000, Icar, 145, 220
Fernández, J. A., Helal, M., & Gallardo, T. 2018, P&SS, 158, 6
Fernández, Y. R., Bauer, J., Kramer, E., et al. 2020, AAS/DPS Meeting, 52, 404.07
Fernández, Y. R., Kelley, M. S., Lamy, P. L., et al. 2013, Icar, 226, 1138
Flaugher, B., Diehl, H. T., Honscheid, K., et al. 2015, AJ, 150, 150
Foster, M. J., Green, S. F., McBride, N., & Davies, J. K. 1999, Icar, 141, 408
Fukugita, M., Ichikawa, T., Gunn, J. E., et al. 1996, AJ, 111, 1748
Gaia Collaboration, Prusti, T., de Bruijne, J. H. J., et al. 2016, A&A, 595, A1
Guilbert-Lepoutre, A. 2012, AJ, 144, 97
Gwyn, S. D. J., Hill, N., & Kavelaars, J. J. 2012, PASP, 124, 579
Hansen, G. B., & McCord, T. B. 2004, JGRE, 109, E01012
Jenniskens, P., & Blake, D. F. 1994, Sci, 265, 753
Jewitt, D. 2009, AJ, 137, 4296
Jewitt, D. 2015, AJ, 150, 201
Jewitt, D., & Kim, Y. 2020, PSJ, 1, 77
Kareta, T., Sharkey, B., Noonan, J., et al. 2019, AJ, 158, 255
Kareta, T., Woodney, L. M., Schambeau, C., et al. 2021, PSJ, 2, 48
Kelley, M. S. P., Woodward, C. E., Bodewits, D., et al. 2016, PASP, 128, 018009
Kouchi, A., & Sirono, S.-i 2001, GeoRL, 28, 827
Laufer, D., Kochavi, E., & Bar-Nun, A. 1987, PhRvB, 36, 9219
Li, J., Jewitt, D., Mutchler, M., Agarwal, J., & Weaver, H. 2020, AJ, 159, 209
Lisse, C., Bar-Nun, A., Laufer, D., et al. 2013, in The Science of Solar System Ices, Astrophysics and Space Science Library, Vol. 356, ed. M. S. Gudipati & J. Castillo-Rogez (New York: Springer), 455
Luu, J. X., & Jewitt, D. C. 1990, AJ, 100, 913
Luu, J. X., & Jewitt, D. C. 1992, Icar, 97, 276
Mazzotta Epifani, E., Palumbo, P., Capria, M. T., et al. 2006, A&A, 460, 935
Mazzotta Epifani, E., Perna, D., Dotto, E., et al. 2017, A&A, 597, A59
Mazzotta Epifani, E., Perna, D., Licandro, J., et al. 2014, A&A, 565, A69
Meech, K. J., Bauer, J. M., & Hainaut, O. R. 1997, A&A, 326, 1268
Meech, K. J., Kleyna, J. T., Hainaut, O., et al. 2017, ApJL, 849, L8
Meech, K. J., & Svoren, J. 2004, in Comets II, ed. M. C. Festou, H. U. Keller, & H. A. Weaver (Tucson, AZ: Univ. Arizona Press), 317
Mommert, M. 2017, A&C, 18, 47
Morbidelli, A., Batygin, K., Brasser, R., & Raymond, S. N. 2020, MNRAS, 497, L46

Morganson, E., Gruendl, R. A., Menanteau, F., et al. 2018, PASP, 130, 074501
Notesco, G., & Bar-Nun, A. 1996, Icarus, 122, 118
Ootsubo, T., Kawakita, H., Hamada, S., et al. 2012, ApJ, 752, 15
Peixinho, N., Boehnhardt, H., Belskaya, I., et al. 2004, Icar, 170, 153
Peixinho, N., Delsanti, A., Guilbert-Lepoutre, A., Gafeira, R., & Lacerda, P. 2012, A&A, 546, A86
Prialnik, D., & Podolak, M. 1995, Icar, 117, 420
Rousselot, P. 2008, A&A, 480, 543
Sarid, G., Volk, K., Steckloff, J. K., et al. 2019, ApJL, 883, 7
Seccull, T., Fraser, W. C., Puzia, T. H., Fitzsimmons, A., & Cupani, G. 2019, AJ, 157, 88
Senay, M. C., & Jewitt, D. 1994, Natur, 371, 229
Shi, J. C., & Ma, Y. H. 2015, MNRAS, 454, 3635
Steckloff, J. K., Graves, K., Hirabayashi, M., Melosh, H. J., & Richardson, J. E. 2016, Icar, 272, 60
Steckloff, J. K., Johnson, B. C., Bowling, T., et al. 2015, Icar, 258, 430
Steckloff, J. K., Sarid, G., Volk, K., et al. 2020, ApJL, 904, L20
Szabó, G. M., Kiss, L. L., & Sárneczky, K. 2008, ApJL, 677, L121
Tiscareno, M. S., & Malhotra, R. 2003, AJ, 126, 3122
Tody, D. 1986, Proc. SPIE, 627, 733
Tody, D. 1993, in ASP Conf. Ser. 52, Astronomical Data Analysis Software and Systems II (San Francisco, CA: ASP), 173
Tonry, J. L., Denneau, L., Flewelling, H., et al. 2018, ApJ, 867, 105
van Dokkum, P. G. 2001a, PASP, 113, 1420
van Dokkum, P. G., Bloom, J., & Tewes, M. 2012, L.A.Cosmic: Laplacian Cosmic Ray Identification, ascl:1207.005
Volk, K., & Malhotra, R. 2008, ApJ, 687, 714
Weiler, M., Rauer, H., Knollenberg, J., Jorda, L., & Helbert, J. 2003, A&A, 403, 313
Weryk, R. J., Lilly, E., Chastel, S., et al. 2016, arXiv:1607.04895
Wierzchos, K., & Womack, M. 2020, AJ, 159, 136
Wierzchos, K., Womack, M., & Sarid, G. 2017, AJ, 153, 230
Womack, M., Sarid, G., & Wierzchos, K. 2017, PASP, 129, 031001
Womack, M., & Stern, S. A. 1997, LPSC, 28, 1575